

Document Version

Final published version

Licence

CC BY

Citation (APA)

Habibi, S., Iqbal, K. T., Costa, P., & Tammisola, O. (2026). Dynamics of oblate particle migration and orientation in duct flows of elastoviscoplastic fluids. *Journal of Fluid Mechanics*, 1032, Article A45. <https://doi.org/10.1017/jfm.2026.11381>

Important note

To cite this publication, please use the final published version (if applicable). Please check the document version above.

Copyright

In case the licence states "Dutch Copyright Act (Article 25fa)", this publication was made available Green Open Access via the TU Delft Institutional Repository pursuant to Dutch Copyright Act (Article 25fa, the Taverne amendment). This provision does not affect copyright ownership.

Unless copyright is transferred by contract or statute, it remains with the copyright holder.

Sharing and reuse





Other than for strictly personal use, it is not permitted to download, forward or distribute the text or part of it, without the consent of the author(s) and/or copyright holder(s), unless the work is under an open content license such as Creative Commons.

Takedown policy

Please contact us and provide details if you believe this document breaches copyrights. We will remove access to the work immediately and investigate your claim.



Dynamics of oblate particle migration and orientation in duct flows of elastoviscoplastic fluids

Shahriar Habibi¹ , Kazi Tassawar Iqbal¹ , Pedro Costa²  and Outi Tammisola¹ 

¹FLOW and SeRC (Swedish e-Science Research Centre), Engineering Mechanics, KTH Royal Institute of Technology, Stockholm, Sweden

²Department of Process & Energy, Delft University of Technology, Delft, The Netherlands

Corresponding author: Shahriar Habibi, shabibi@kth.se

(Received 1 August 2025; revised 20 January 2026; accepted 23 February 2026)

Elastoviscoplastic (EVP) fluids, characterised by the coexistence of elastic, viscous and yield-stress properties, play a central role in diverse applications, including drug delivery, 3D printing and hydraulic fracturing. These fluids often transport non-spherical particles whose migration dynamics strongly influences flow behaviour. In this work, we employ interface-resolved direct numerical simulations to investigate the migration and orientation dynamics of finite-size spheroidal particles suspended in EVP duct flows across a wide range of governing parameters. Our results show that the equilibrium position and orientation of the particles are influenced significantly by both their aspect ratio and the carrier fluid rheology. In Saramito fluids, spheroidal particles migrate towards the duct centre and align along the duct diagonals in the presence of inertia. At sufficiently high elasticity, they penetrate the central plug and reach the duct core, irrespective of their initial position or shape. At lower elasticities, where larger plug regions persist, interactions with the plug alter the angular dynamics of the particles, leading to unsteady, quasi-periodic tumbling and spinning motions. In contrast, in Saramito–Giesekus fluids, the interplay between inertial forces, shear-thinning plastic viscosity and yield stress drives particles towards the duct corners, aligning them perpendicular to the duct diagonals. In semi-dilute suspensions, flattened particles maintain a greater distance from the walls, whereas their spherical counterparts tend to cluster directly at the corners. These findings reveal complex migration and orientation behaviours unique to EVP media and suggest new opportunities for geometry-based particle separation in microfluidic applications.

Key words: microfluidics, multiphase and particle-laden flows, non-Newtonian flows

1. Introduction

Elastoviscoplastic (EVP) fluids are a category of non-Newtonian materials that exhibit a dual behaviour: they act like viscoelastic solids when subjected to shear stresses below a critical yield stress, but transform into a fluid-like state once this stress threshold is exceeded (Balmforth, Frigaard & Ovarlez 2014; Saramito 2016; Ewoldt & McKinley 2017). These fluids are frequently combined with particles and are utilised in various industrial and scientific contexts, including hydraulic fracturing in the oil industry (Barbati *et al.* 2016), the pumping of concrete in the construction industry (Fataei 2022), transportation of slurries (Li *et al.* 2020), 3-D printing (Eom *et al.* 2025) and the development of biomaterials for drug delivery (Gratton *et al.* 2008; Mitragotri & Lahann 2009). In many applications, the suspended particles are non-spherical, adding significant complexity to the suspension dynamics. Even for simple spheroidal shapes, particle orientation introduces an additional degree of freedom, leading to intricate particle–fluid and particle–particle interactions (Gunes *et al.* 2008; Dabade, Marath & Subramanian 2015; Rosén 2016; Voth & Soldati 2017). Oblate (flattened, disk-shaped) and prolate (elongated, rod-shaped) spheroids are widely used as canonical representations of non-spherical particles, relevant to a broad range of biomedical and industrial applications, from red blood cells and platelets to synthetic fibres and engineered micro-/nano-particles (Amini *et al.* 2014).

A major breakthrough in the dynamics of non-spherical particles was achieved through Jeffery’s pioneering study (Jeffery 1922) on the angular dynamics of ellipsoidal particles in unbounded shear flow at low Reynolds numbers. This work led to the identification of the Jeffery orbit, where an ellipsoid undergoes a combination of rotation and tumbling, following closed trajectories determined by its aspect ratio and initial orientation. Subsequent studies explored how particle inertia (Saffman 1956; Rosén *et al.* 2014; Einarsson *et al.* 2015; Di Giusto *et al.* 2024), and the rheology of the carrier medium (e.g. shear-thinning viscosity (Abtahi & Elfring 2019; Li *et al.* 2023a), or viscoelasticity (Leal 1975; D’Avino *et al.* 2014; Wang, Yu & Lin 2019; Li *et al.* 2023b) influence Jeffery orbits. While these studies provided valuable insights into the angular dynamics of spheroids in Couette flows, many practical applications – such as cell focusing techniques (Di Carlo *et al.* 2007) – typically involve Poiseuille duct flows, where particles experience both rotation and lateral migration.

The seminal work of Segré & Silberberg (1961) established that in a dilute suspension of spherical particles with inertia, initially randomly distributed, the particles gradually migrate across streamlines to reach a stable configuration, forming a narrow ring approximately 0.6 times the tube radius from the centre (Segré & Silberberg 1962; Matas, Morris & Guazzelli 2004). Similarly, in square or rectangular duct flows of Newtonian fluids, spheres tend to accumulate along the centre of the duct walls, at a distance of approximately 0.3 times the channel width from the cross-sectional centre (Chun & Ladd 2006; Di Carlo 2009; Choi, Seo & Lee 2011; Miura, Itano & Sugihara-Seki 2014; Kazerooni *et al.* 2017). In a laminar Newtonian flow, the particle equilibrium position is determined by the competition between two opposing inertial forces: the shear-gradient lift, which drives particles away from the centreline (Ho & Leal 1974; Asmolov 1999), and the wall-induced lift, which pushes them towards the channel centre (Zeng, Balachandar & Fischer 2005; Martel & Toner 2014). This type of migration was later analysed in the context of non-spherical particles (Hur *et al.* 2011; Masaeli *et al.* 2012; Uspal, Burak Eral & Doyle 2013; Takeishi & Imai 2017). The cross-streamline migration of oblate particles in square ducts resembles that of spheres, exhibiting similar equilibrium positions and manifolds. However, unlike spheres, spheroidal particles tumble during migration, resulting in non-uniform lateral trajectories and longer downstream focusing lengths (Lashgari *et al.* 2017; Hafemann & Fröhlich 2023). Additionally, spheroids with higher

aspect ratios (more elongated) tend to have their centres closer to the duct mid-plane at equilibrium (Lashgari *et al.* 2017).

The rheological properties of the carrier fluid represent another critical factor influencing the dynamics of particle migration (Bartram, Goldsmith & Mason 1975; Won & Kim 2004; Leshansky *et al.* 2007; Stoecklein & Di Carlo 2018; Shaqfeh 2019; Tanriverdi *et al.* 2025). Even in flows with negligible inertia ($Re \simeq 0$), the presence of viscoelasticity can induce cross-streamline migration of particles, unlike in Newtonian fluids where no migration occurs in creeping flows (Gauthier, Goldsmith & Mason 1971; Lormand & Phillips 2004; D'Avino *et al.* 2017). Note that the Reynolds number, $Re = \rho VL/\mu$, represents the ratio of inertial to viscous forces, where ρ is the fluid density, V is a characteristic velocity, L is a characteristic length, and μ is the dynamic viscosity. Indeed, the interplay between inertia and elasticity complicates the particle migration dynamics significantly, as discussed by Li, McKinley & Ardekani (2015) and Tanriverdi *et al.* (2024). In the context of non-spherical particles in viscoelastic media, Tai *et al.* (2020*a,b*) derived approximate analytical expressions for the viscoelastic force and torque acting on arbitrarily shaped particles suspended in a general quadratic flow. These studies, based on a second-order fluid model, were limited to weakly viscoelastic regimes characterised by slow, gradual deformations. The authors found that spheroidal particles tend to align their long axes with the vorticity direction, although finite aspect ratios lead to deviations from predictions for slender bodies. Furthermore, scaling analyses reveal that the lift experienced by prolate particles initially exceeds that of spheres, but diminishes as the particles transition to a log-rolling state near the channel centre. This behaviour ultimately results in a reduced average migration velocity for more elongated particles. Subsequent experimental work by the same authors (Tai & Narsimhan 2022) confirmed these theoretical predictions, notably showing that spherical particles migrate laterally faster than spheroids.

Langella *et al.* (2023) experimentally studied the lateral migration of prolate particles in a viscoelastic fluid flowing through a microchannel under creeping flow conditions. At relatively low flow rates, where the particles experience the constant-viscosity regime of the fluid, viscoelasticity drives the spheroids towards the channel centre without inducing a preferential orientation. More recently, Hu *et al.* (2024) investigated numerically the elasto-inertial migration of a neutrally buoyant spheroid in Oldroyd-B viscoelastic duct flows. The authors identified distinct rotational modes of spheroidal particles and demonstrated that, by tuning the elastic number near a critical threshold, spheroids with varying aspect ratios can be effectively separated. Furthermore, Li, Xu & Zhao (2024) showed that, unlike spherical particles, oblate spheroids undergo oscillatory cross-stream migration within the duct, driven by orientation-dependent lift forces. They also identified a critical elastic number that controls the migration efficiency of oblate particles in such flows. The elasto-inertial migration of spheroidal particles has been extensively utilised in various microfluidics and biological applications (Liu *et al.* 2015; Lu *et al.* 2015; Liu *et al.* 2022).

While much of the existing literature has focused on flows dominated by either inertia or elasticity, the combined influence of elasticity and yield stress remains less explored, despite its potential to produce unique particle behaviours (Putz *et al.* 2008; Cheddadi *et al.* 2011; Holenberg *et al.* 2012; Fraggidakis, Dimakopoulos & Tsamopoulos 2016; Lopez *et al.* 2018; Izbassarov & Tammisola 2020; Pourzahedi, Zare & Frigaard 2021; Habibi 2026). For example, Chaparian *et al.* (2020*a*) showed that, in EVP channel flows, a single sphere can penetrate the central plug and reach the centreline at specific Weissenberg and Reynolds numbers, in contrast to purely viscoelastic cases where particles tend to remain off centre. Complementing this, Zade *et al.* (2020) experimentally demonstrated that inertia modulates migration patterns in Carbopol duct flows: at low inertia, particles cluster

near the corners, while at higher inertia, they distribute in a circular pattern between the duct centre and the walls. More recently, Habibi *et al.* (2025) investigated the dynamics of spherical particle suspensions in duct flows of EVP fluids via direct numerical simulations. They discovered that increasing the yield stress of the fluid promotes particle migration towards the duct corners in EVP fluids with shear-thinning plastic viscosity, as a result of the yield stress amplifying the first normal stress difference. They also found that particle-induced stresses can disrupt the central plug region, leading to the formation of separated islands of unyielded areas in the EVP flow.

While a limited number of studies have investigated the migration of spherical particles in EVP flows, the complex interplay between the particle dynamics and EVP fluid rheology remains poorly understood. This knowledge gap is even more pronounced for non-spherical particles, which more accurately represent those encountered in practical applications spanning biomedical, industrial and geophysical systems. The anisotropic geometry of these particles introduces additional complexity, giving rise to distinct migration patterns, orientation dynamics and clustering behaviour influenced by both particle shape and the rheological properties of the carrier fluid. To address this, we perform fully resolved, three-dimensional direct numerical simulations (DNS) of spheroidal particles in pressure-driven EVP duct flows. Our simulations systematically investigate the influence of particle shape, inertia, volume fraction and key rheological parameters – including yield stress, elasticity and shear-thinning viscosity – on both the transient evolution and the final spatial distribution and orientation of particles. Additionally, we compare the behaviour of spheroidal and spherical particles to explore potential opportunities for shape-based particle separation in EVP carrier fluids.

The remainder of this paper is organised as follows. The problem formulation and corresponding non-dimensional numbers are outlined in § 2. Next, the governing equations for the fluid and particles, along with the numerical methods, are presented in § 2.1 and § 2.2. The simulation results concerning the migration and orientation of spheroidal particles within EVP fluids are discussed in § 3. Finally, the key conclusions of this study are presented in § 4.

2. Problem statement

We investigate numerically the behaviour of non-colloidal rigid spheroidal particles with an equivalent diameter D , suspended in a laminar EVP fluid flowing through a straight duct with a square cross-section. The equivalent diameter is defined as $D = 2(ab^2)^{1/3}$, where a and b are the semi-major and semi-minor axes of the spheroids. The particles are either spherical, oblate spheroids (lentil-like), or prolate spheroids (rugby ball-shaped). Simulations are performed in a Cartesian domain of dimensions $L_x = 2H$, $L_y = 6H$ and $L_z = 2H$, where H is the half-height of the square-duct cross-section, and y , z and x denote the streamwise, vertical and spanwise directions, respectively (see figure 1). Particles are initially at rest and randomly distributed and oriented throughout the domain. The blockage ratio, defined as $\kappa = D/(2H)$, is set to 0.25 in most cases; additional simulations with $\kappa = 0.2$ and $\kappa = 0.125$ are conducted to examine particle size effects. Brownian motion is neglected, as the particles are assumed large enough for thermal fluctuations to be insignificant. In addition, all particles are neutrally buoyant, with densities equal to that of the surrounding fluid. In what follows, the velocity is non-dimensionalised by the bulk flow velocity V_b , length by the half-height of the channel H and time by H/V_b . Pressure and the extra stress tensor are scaled by ρV_b^2 . Note that the total viscosity of the material (μ) is the sum of the solvent and polymer viscosities ($\mu = \mu_s + \mu_p$). The key non-dimensional parameters governing the system are summarised in

Group	Definition	Interpretation
Reynolds number (Re)	$\rho V H / \mu$	Ratio of the inertial to viscous forces
Weissenberg number (Wi)	$\lambda V / H$	Proportion between elastic and viscous forces
Elasticity number (El)	$Wi / Re = \lambda \mu / \rho H^2$	Ratio of elastic force to inertial force
Bingham number (Bi)	$\tau_y H / \mu V$	Proportion between yield stress and viscous stress
Particle volume fraction (ϕ)	$\pi N D^3 / (6 L_x L_y L_z)$	Ratio of the particles to total volume
Viscosity ratio (β)	μ_s / μ	Ratio of solvent viscosity to total viscosity
Blockage ratio (κ)	$D / (2H)$	Ratio of particle diameter to duct height
Aspect ratio (AR)	a / b	Ratio of the spheroid major axis to its minor axis
Mobility parameter	α	Mobility parameter (shear-thinning factor)

Table 1. Non-dimensional numbers in the problem of spheroidal particle suspension in EVP duct flows.

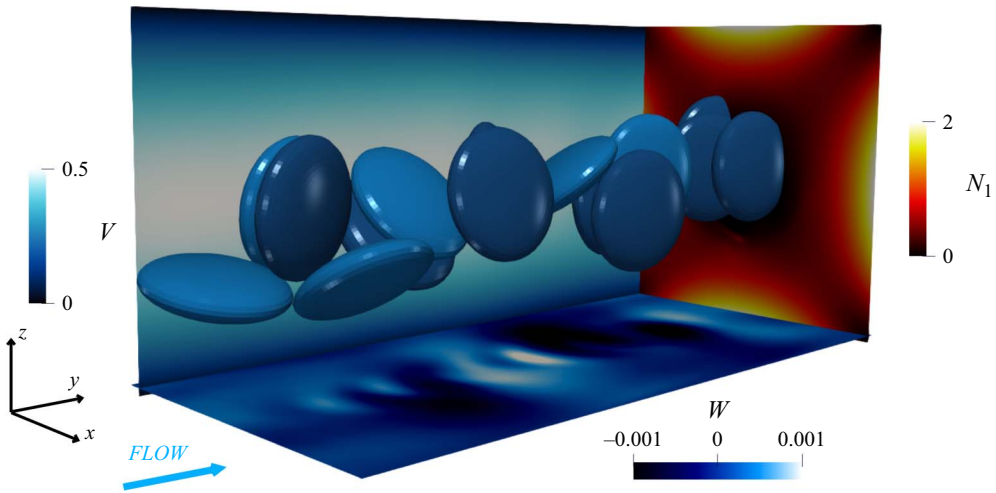


Figure 1. Three-dimensional view of the computational domain with solid volume fraction $\phi = 6\%$. Trains of oblate particles are formed at the duct core due to the particle migration towards the centre. Velocity distributions are provided for the streamwise direction (on the yz -plane) and the z -direction (on the xy -plane), with N_1 showing the first normal stress difference in the xz -plane. Particle colours are for illustrative purposes only.

table 1, where τ_y is the yield stress, λ is the relaxation time of the EVP fluid, N is the number of particles and L_x , L_y and L_z are the duct dimensions in each direction.

The computational domain (see figure 1) is discretised using $160 \times 480 \times 160$ Eulerian grid points (for the $\kappa = 0.2$) along the spanwise (x), streamwise (y) and vertical (z) directions, respectively. Each spheroidal particle is resolved using 32 Eulerian grid points across its equivalent diameter, with surface discretisation comprising 3720 (oblate), 3610 (prolate) and 3219 (spherical) uniformly distributed Lagrangian points. This level of resolution is chosen in order to properly resolve the fluid–particle interactions. All simulations are conducted at a constant bulk velocity V_b , which in most cases corresponds to a fixed Reynolds number $Re = 20$. Periodic boundary conditions are applied to both the fluid and particles in the streamwise direction, while no-slip and no-penetration conditions are enforced on the remaining domain boundaries. While wall slip is a characteristic feature of yield-stress fluid flows (Péméja *et al.* 2019; Younes *et al.* 2020), the present study assumes a no-slip boundary condition. This choice is motivated by our

previous investigations (Habibi *et al.* 2025), which demonstrated excellent agreement with experimental data for particle suspensions in Carbopol under the no-slip assumption (Zade *et al.* 2020). Furthermore, the no-slip condition isolates the influence of bulk rheology and precludes the introduction of additional unconstrained empirical parameters associated with slip models.

2.1. Governing equations

The dynamics of the suspending fluid is described by the incompressible Navier–Stokes equations, subject to mass and momentum conservation

$$\nabla \cdot \mathbf{u} = 0, \tag{2.1}$$

$$\frac{\partial \mathbf{u}}{\partial t} + (\mathbf{u} \cdot \nabla) \mathbf{u} = -\nabla p + \frac{\beta_s}{Re} \nabla^2 \mathbf{u} + \nabla \cdot \boldsymbol{\tau}^p + \mathbf{f}. \tag{2.2}$$

Here, \mathbf{u} and p denote the velocity and pressure fields, respectively, while $\boldsymbol{\tau}^p$ represents the polymeric stress tensor and Re is the Reynolds number. The term \mathbf{f} on the right-hand side of the momentum conservation accounts for the immersed boundary force, which captures particle-fluid interactions (detailed in § 2.2). The total stress tensor is composed of Newtonian solvent and polymeric contributions: $\boldsymbol{\tau} = \boldsymbol{\tau}^s + \boldsymbol{\tau}^p$, where $\boldsymbol{\tau}^s = \beta_s (\nabla \mathbf{u} + \nabla \mathbf{u}^T)$, and $\beta_s = \mu_s / \mu$ denotes the viscosity ratio. In all simulations, β_s is fixed at 0.1. To model the non-Newtonian behaviour of the EVP fluid, we employ the Giesekus (Giesekus 1982) modification of the Saramito equation (Saramito 2007) to capture the second normal stress difference and the shear-thinning viscosity of the EVP carrier fluid

$$Wi \overset{\nabla}{\boldsymbol{\tau}}^p + F \left(\boldsymbol{\tau}^p + \frac{Wi \alpha}{(1 - \beta_s)} (\boldsymbol{\tau}^p \cdot \boldsymbol{\tau}^p) \right) = \frac{2(1 - \beta_s)}{Re} \mathbf{D}, \tag{2.3}$$

Here, Wi denotes the Weissenberg number, defined in table 1, and the function $F = \max(0, (|\boldsymbol{\tau}_d^p| - Bi/Re)/|\boldsymbol{\tau}_d^p|)$ accounts for the presence of yield stress in the Saramito model where Bi denotes the Bingham number. The term $|\boldsymbol{\tau}_d^p| \equiv \sqrt{\boldsymbol{\tau}_d^p : \boldsymbol{\tau}_d^p / 2}$, where $\boldsymbol{\tau}_d^p = \boldsymbol{\tau}^p - (\text{tr } \boldsymbol{\tau}^p / \text{tr } \mathbf{I}) \mathbf{I}$, defines the deviatoric part of $\boldsymbol{\tau}^p$, and \mathbf{I} denotes the identity tensor. The shear-thinning behaviour is modelled through the mobility parameter α with $0 < \alpha < 1$. When $\alpha = 0$, the model reduces to the Saramito EVP model, and if both $\alpha = 0$ and $Bi = 0$, it recovers the Oldroyd-B viscoelastic model (Oldroyd 1950). Note that $\overset{\nabla}{\boldsymbol{\tau}}^p$ represents the upper-convected time derivative of the polymer stress tensor, defined as (Oldroyd 1950)

$$\overset{\nabla}{\boldsymbol{\tau}}^p \equiv \frac{\partial \boldsymbol{\tau}^p}{\partial t} + \mathbf{u} \cdot \nabla \boldsymbol{\tau}^p - \nabla \mathbf{u}^T \cdot \boldsymbol{\tau}^p - \boldsymbol{\tau}^p \cdot \nabla \mathbf{u}. \tag{2.4}$$

The translational and rotational dynamics of each particle is governed by the Newton–Euler equations

$$\rho_p V_p \frac{d\mathbf{u}_p}{dt} = \oint_{\partial V} \boldsymbol{\sigma} \cdot \mathbf{n} \, dA + \mathbf{F}_c, \tag{2.5}$$

$$\frac{d(I_p \boldsymbol{\omega}_p)}{dt} = \oint_{\partial V} \mathbf{r} \times (\boldsymbol{\sigma} \cdot \mathbf{n}) \, dA + \mathbf{T}_c, \tag{2.6}$$

where \mathbf{u}_p and $\boldsymbol{\omega}_p$ are the linear and angular velocities of the particle, ρ_p , V_p and I_p are its density, volume and moment of inertia, respectively. The particle domain is denoted by ∂V and the position vector relative to the particle centre by \mathbf{r} . Note that the Cauchy stress tensor is expressed as $\boldsymbol{\sigma} = -p\mathbf{I} + \boldsymbol{\tau}^p + \beta_s (\nabla \mathbf{u} + \nabla \mathbf{u}^T)$. Collision forces and torques due

to particle–particle and particle–wall interactions are represented by F_c and T_c . These short-range interactions are modelled using a soft-sphere collision framework with a lubrication correction, following Costa *et al.* (2015) for spherical and Ardekani *et al.* (2016) for spheroidal particles. Further details regarding the lubrication correction and the collision model are provided in [Appendix C](#).

2.2. Numerical method

The numerical framework employs a direct-forcing immersed boundary method (IBM), in which the particles are represented by moving Lagrangian grids interacting with the fluid field defined on a stationary Eulerian mesh. The governing momentum and constitutive equations for the carrier fluid are discretised using a finite-difference scheme. To solve the fluid momentum equations, a projection method is used to decouple pressure and velocity, with the pressure Poisson equation efficiently handled by a scalable Fast Fourier Transform-based solver (Costa 2018). Spatial derivatives are primarily computed using central finite differences, except for the advective term in the constitutive equation, which is treated with a fifth-order weighted essentially non-oscillatory scheme (Shu 2009). Temporal integration of all governing equations is performed using a third-order Runge–Kutta method. The code is parallelised in two spatial directions using pencil-based domain decomposition and the Message Passing Interface framework, with a manager–worker communication strategy optimising particle data exchange and load balancing (Costa 2018).

The fluid–solid interaction is modelled using the direct-forcing IBM algorithm proposed by Breugem (2012) and later extended to ellipsoidal particles by Ardekani *et al.* (2016), incorporating lubrication, friction and collision models to capture short-range particle interactions. In the present study, we adopt this numerical framework to simulate suspensions of oblate and prolate spheroidal particles in EVP duct flows. The simulations are more computationally demanding than those with spherical particles (Habibi *et al.* 2025) due to the need to update each particle moment of inertia at every time step. In the IBM, the fluid domain is discretised using a uniform staggered Cartesian grid ($\Delta x = \Delta y = \Delta z$), while the particle surfaces are represented by a set of uniformly spaced Lagrangian markers that move with the interface. The fluid momentum equations are solved over the entire Eulerian grid, and the influence of immersed particles is incorporated by introducing a localised forcing term, \mathbf{f} , on the right-hand side of the momentum conservation equation (2.2). This force satisfies the no-slip and no-penetration boundary conditions at the particle surface by acting near the fluid–solid interface (Mittal & Iaccarino 2005). The computed immersed boundary force is applied to both the fluid and the particles to advance their motion in time. Further details of the numerical framework can be found in our earlier studies (Ardekani *et al.* 2016; Izbassarov *et al.* 2018; Niazi Ardekani 2019). Note that we performed box size and resolution studies to ensure the reported results are free from numerical artefacts (see [Appendix A](#)). Additionally, both the IBM and EVP fluid solvers were validated through separate test cases (see [Appendix A](#)). Due to the fine resolution and slow particle migration dynamics, simulations are computationally intensive, with some cases requiring up to six weeks on 32 processor cores, depending on the focusing distance needed to reach steady state.

3. Results

This section presents numerical simulations of the spheroidal particle dynamics in EVP duct flows. We first examine results for particle migration and orientation across a range of carrier fluids, including Newtonian, viscoplastic (VP), viscoelastic (VE) and EVP models.

ϕ (%)	Re	Bi	El	α	κ	$L_x \times L_y \times L_z$
[0–6]	[10–40]	[0–1]	[0–0.1]	[0–0.3]	[0.125–0.25]	[4 × 12 × 4]

Table 2. Summary of the non-dimensional parameters explored in our simulations. Domain dimensions L_x , L_y and L_z are expressed in units of the particle diameter for $\kappa = 0.25$. For cases with lower κ , the domain dimensions increase proportionally.

These cases establish a baseline within our numerical framework, allowing the specific effects of EVP rheology to be distinguished from simpler constitutive models. In § 3.2, we discuss particle migration in VE duct flows in greater detail. We then extend the analysis to EVP fluids and shear-thinning yield-stress fluids in § 3.3 and § 3.4, respectively. Finally, in § 3.5, we examine the collective behaviour of spheroidal particles in EVP fluids for dilute and semi-dilute suspensions. A summary of the simulation cases performed in this study is provided in table 2.

3.1. Influence of fluid rheology on lateral migration

We first examine the migration behaviour of oblate particles in Newtonian ($El = 0$, $Bi = 0$), VE ($El = 0.05$, $Bi = 0$), VP ($El = 0$, $Bi = 1$) and EVP ($El = 0.05$, $Bi = 1$) duct flows (see table 1 for the definition of elasticity number El and Bingham number Bi). The VE fluid is modelled by the Oldroyd-B equation (with $Bi = 0$ and $\alpha = 0$ in (2.3)), while the EVP fluid is modelled using the Saramito constitutive equation ($\alpha = 0$ in (2.3)). The VP fluid is modelled by considering a negligible elasticity in the Saramito model, thus approximating the Bingham plastic model. Figure 2(a) depicts a cross-section of the square duct, with each quadrant corresponding to one of the carrier fluids. Dashed ellipses denote the initial positions and orientations of the particles projected onto the cross-section, and solid ellipses indicate their final states. The lines connecting these two states represent particle trajectories in the duct cross-section (xz -plane). Insufficient shear stress at the duct centre in yield-stress fluids leads to an unyielded plug, shown as circles in the VP and EVP quadrants. The simulations are conducted at a fixed Reynolds number of 20 and a blockage ratio of 0.25. The aspect ratio of the oblate particles is set to 1/3. In addition, the orientation of the oblate particle is described by the unit vector $\mathbf{n} = [n_x, n_y, n_z]$, aligned with its symmetry axis. Similarly, the rotation of the particle is characterised by the vector $\boldsymbol{\omega} = [\omega_x, \omega_y, \omega_z]$. In all simulations, the particle is initially oriented with $\mathbf{n} = [0, 0, 1]$, so that its symmetry axis is aligned with the vertical direction (z), while both its initial velocity and rotation are set to zero.

In the Newtonian case, the particle tends to stay away from the walls due to wall-repulsion forces and migrates slightly towards the duct centre while aligning along the diagonal. This behaviour is consistent with the observations of Lashgari *et al.* (2017) regarding the migration of oblate particles with high aspect ratios ($\kappa \geq 0.25$) in Newtonian duct flows. In the VP case, the particle exhibits negligible migration towards the centre but still aligns along the diagonal. This limited migration results from repulsion from both the duct walls and the central plug. The role of the plug in hindering particle migration towards the centre is discussed in detail in § 3.3. In contrast to the Newtonian and VP fluids, the migration behaviour in the VE and EVP cases is markedly different: the particle migrates towards and ultimately reaches the duct centre.

Figure 2(b) shows the time evolution of the z -component of the orientation vector, n_z , for selected cases. The colours correspond to those in panel (a). In the Newtonian case, after an initial transient during which the particle undergoes tumbling motion, it rapidly

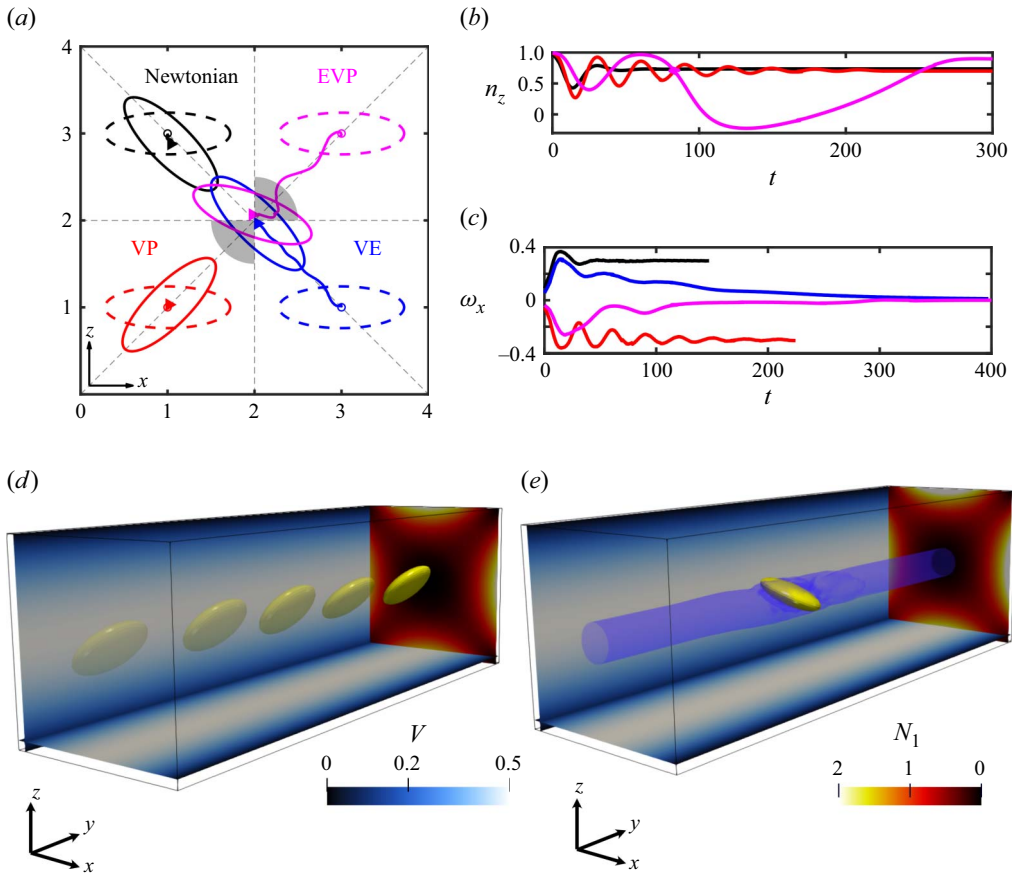


Figure 2. (a) Lateral trajectories of an oblate particle (with an aspect ratio of $AR = 1/3$) in a square duct, with each quadrant corresponding to a different carrier fluid: Newtonian, VP, VE and EVP. Circles and triangles indicate initial and equilibrium positions, while dashed and solid ellipses denote initial and final orientations, respectively. (b) Orientation of the oblate symmetry axis along the z -axis as a function of non-dimensional time. (c) Temporal evolution of the oblate angular velocity along the spanwise direction (ω_x). (d) Three-dimensional visualisation of the motion of a single oblate particle in a VE duct flow. (e) Instantaneous snapshot of the flow field with the oblate particle in EVP duct flow. The first normal stress difference, N_1 , is shown in the xz -plane, while the contours in the xy - and yz -planes represent the streamwise velocity component (V). The central plug region is illustrated in purple.

reaches a steady orientation of $\mathbf{n} = [0.7, 0, 0.7]$. In the VP case, the particle exhibits pronounced tumbling before its rotation gradually damps, ultimately achieving a steady diagonal orientation similar to the Newtonian case. In contrast, in the EVP case, the orientation dynamics exhibits a long transient and strong tumbling due to interactions with the central plug region. The particle then yields the central region, ultimately becoming fully trapped around $t \approx 280$, with a steady orientation of $n_z = 0.9$.

Furthermore, figure 2(c) shows the time evolution of the angular velocity of the oblate particle around the spanwise (x) axis. Since the particles settle in a diagonal orientation in the Newtonian, VP and VE cases, ω_x and ω_z exhibit similar behaviour, indicating rotation about the shortest axis (spin). After the initial tumbling motion in the VE and EVP cases, ω_x decays to zero, indicating that spinning ceases at equilibrium. In contrast, for the Newtonian and VP fluids, steady spinning persists, even though the particle orientation about the y -axis remains aligned along the duct diagonals (i.e. $\omega_y = 0$).

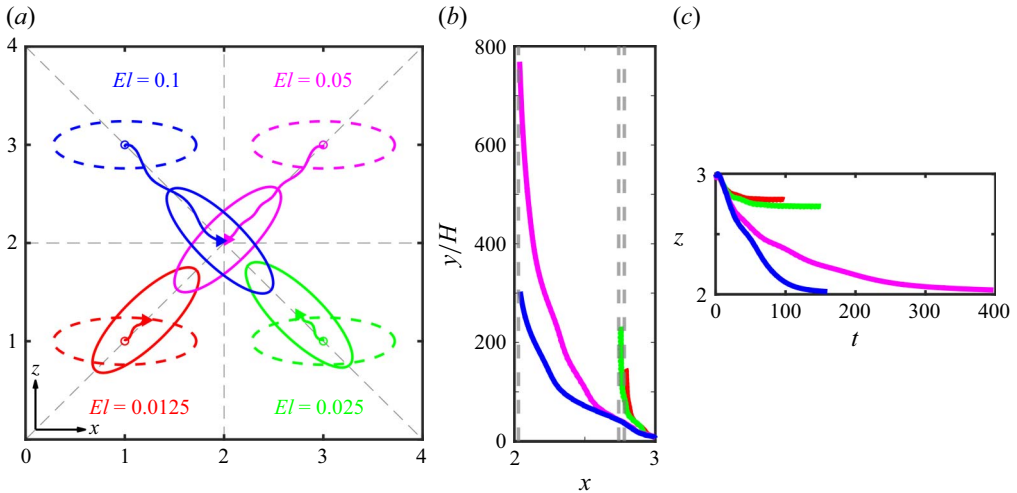


Figure 3. (a) Migration trajectories of oblate particles in VE duct flows with varying fluid elasticity ($El = 0.012$ to 0.1) shown in the xz -plane. Dashed ellipses indicate the initial position and orientation, while solid lines mark the final state. (b) Focusing length versus particle spanwise position, where vertical dashed lines indicate the equilibrium positions. (c) Vertical particle position over time for different elasticity values. For ease of comparison particles start from the same vertical position.

To further examine the spatial distribution of particles within the duct, panels (c) and (d) show three-dimensional (3-D) instantaneous snapshots of the flow field and the oblate particle in the VE and EVP fluids, captured after the particle dynamics reached a steady state. In both cases, the cross-section in the xz -plane displays the distribution of the first normal stress difference ($N_1 = \tau_{yy} - \tau_{zz}$), while the yz - and xy -planes illustrate contours of the streamwise velocity. In the EVP flow, the central plug region is highlighted in purple, indicating that the oblate particle is trapped within the plug and is transported together with it.

The presence of VE normal stresses is the primary reason for the distinct particle migration observed in VE and EVP fluids compared with non-elastic cases such as Newtonian and VP flows. As depicted in the 3-D snapshots for both VE and EVP flows, N_1 exhibits maxima near the walls ($N_1 = 2$) and minima at the centre and corners ($N_1 = 0$). This non-uniform distribution generates an asymmetric elastic force that drives particles towards the duct centre (Ho & Leal 1976; Zhou & Papautsky 2020). As a result, particles can overcome inertial forces and migrate towards the duct centre, depending on the local N_1 gradient.

In the following subsections, we present the details of the particle dynamics in VE (§ 3.2) and EVP fluids (§ 3.3 and § 3.4) and elaborate on the role of the governing parameters in particle migration and orientation.

3.2. Viscoelastic carrier fluid

Here, we examine the migration behaviour of oblate particles in a VE duct flow, modelled by the Oldroyd–B equation ($Bi = 0$ and $\alpha = 0$). Figure 3(a) shows a cross-section of the square duct, including the initial and final particle positions and orientations, as well as the particle trajectories in the duct cross-section (xz -plane). Simulations are conducted at a fixed Reynolds number of $Re = 20$ and a blockage ratio of 0.25 , employing oblate particles with an aspect ratio of $1/3$.

To investigate the effect of fluid elasticity on particle migration and orientation, the elasticity number (El) is varied systematically between 0.01 and 0.1 , with each quadrant

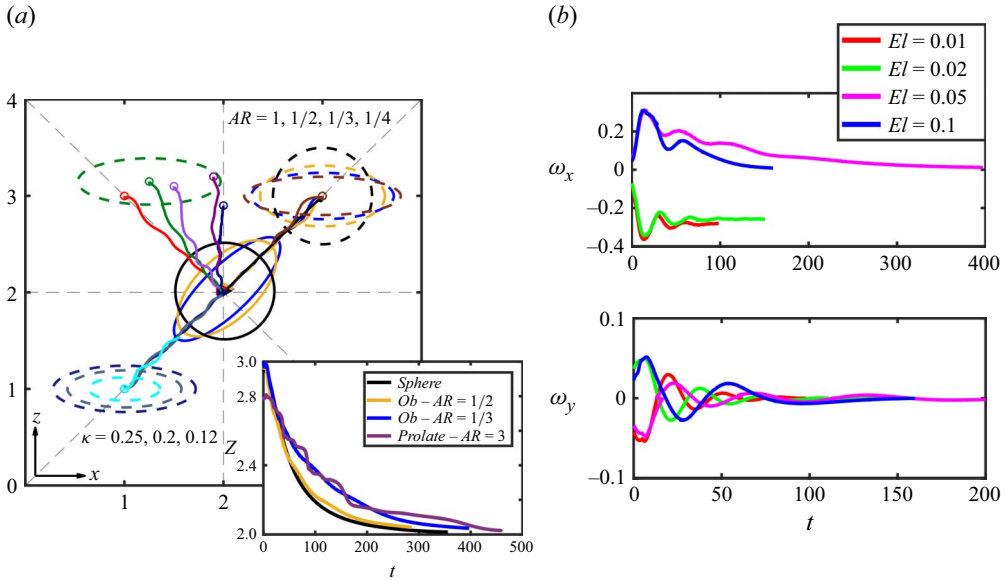


Figure 4. (a) Cross-sectional trajectories of oblates with aspect ratios ranging from 1/4 to 1, confinement ratios from 0.125 to 0.25 and different initial positions. The inset of the figure shows the vertical particle position over time for various particle shapes. (b) Time evolution of the angular velocity of the oblate with $AR = 1/3$ along the streamwise (y) and spanwise (x) directions at $El = 0.01-0.1$.

in figure 3(a) corresponding to one of these elasticity values. In all cases, the particles migrate towards the duct core and align with the diagonal symmetry line within their respective quadrants. In carrier fluids with low elasticity ($El < 0.05$), particles migrate only partially towards the duct centre, settling at intermediate positions between the centre and the corners. In contrast, at higher elasticities ($El \geq 0.05$), particles complete their migration to the duct core. Figure 3(b) shows the focusing length (y/H) – defined as the downstream distance required for oblates to reach their equilibrium position – plotted against their initial lateral offset from the duct centreline. Trajectories are colour coded consistently with panel (a). For the initial positions considered here, lower elasticity appears to yield shorter focusing lengths (e.g. the particle in $El = 0.0125$ focuses within approximately 180 channel heights, compared with roughly 800 and 300 for $El = 0.05$ and $El = 0.1$, at the same bulk Reynolds number). This trend is primarily due to the proximity of the release points to the respective equilibrium positions; the ordering of the focusing lengths may reverse if particles are instead introduced near the centreline.

To investigate this further, we plot the vertical position of oblate particles versus time in figure 3(c). The results reveal that particles in fluids with lower elasticity ($El = 0.0125$ and 0.025) reach equilibrium more quickly, as they have a partial migration and travel a shorter distance to their equilibrium position. In contrast, at higher elasticity, particles fully migrate to the centreline, with faster migration observed in the $El = 0.1$ case compared with $El = 0.05$.

This migration behaviour appears robust across various initial positions, particle sizes and aspect ratios, as illustrated in figure 4(a). The figure shows oblates with aspect ratios ranging from 1/4 (highly elongated) to 1 (spherical), all having the same equivalent diameter of 1 and suspended in a fluid with fixed elasticity of $El = 0.05$. Owing to the geometric symmetry of the square duct, initial particle positions are sampled across only one eighth of the cross-sectional area. Regardless of initial conditions, all particles

ultimately migrate towards the duct centre. The spherical particle follows a linear path (black line in [figure 4\(a\)](#)) because its initial position lies on the diagonal, and the geometric symmetry of the configuration preserves a straight trajectory. In contrast, non-spherical particles break this symmetry through their rotational and tumbling motions, resulting in the oscillatory lateral trajectories observed in [figure 4\(a\)](#) (Li *et al.* 2024). This behaviour is further quantified in the inset of [figure 4\(a\)](#), which plots the vertical position of various particle shapes over time. Among them, the sphere demonstrates the fastest lateral migration, whereas the prolate particle with $AR = 3$ migrates the slowest. This behaviour is due to the ongoing reorientation of oblate and prolate particles along Jeffery-like orbits (Jeffery 1922), causing trajectory and velocity oscillations that delay their migration to the centre. Note that at the initial stage of motion, the oblate particle with $AR = 1/2$ and the prolate particle experience faster migration (higher lift) compared with the spherical particle, although overall, the spherical particle exhibits the highest migration velocity among them. Irrespective of shape, the particles ultimately align to minimise their projected surface area in the streamwise direction. For example, the oblates ($AR = 1/2$ or $1/3$) adopt a diagonal orientation to reduce drag.

The angular velocity of the oblate particles with $AR = 1/3$ around the streamwise axis (ω_y) for different elasticity numbers is shown in [figure 4\(b\)](#). The particles exhibit Jeffery-like orbits, with oscillations in angular velocity that gradually decay to zero, indicating convergence to a stable orientation aligned with the duct diagonal. While any orientation with the minor axis lying in the xz -plane results in the same projected area in the streamwise direction, the diagonal alignment is preferred because it maximises the distance between the particle surface and the duct walls, reducing wall-induced hydrodynamic interactions (Lashgari *et al.* 2017). In this way, the particle simultaneously minimises drag and avoids near-wall confinement, leading to the observed equilibrium orientation. Comparing ω_y for different elasticity numbers shows that the oscillation amplitude decreases as fluid elasticity increases. For example, the peak ω_y drops from 0.078 at $El = 0.012$ to 0.053 at $El = 0.1$. This reduction is due to VE stresses that dampen particle rotation, consistent with the findings of Snijkers *et al.* (2011) for spherical particles. Furthermore, [figure 4\(b\)](#) shows the angular velocity of oblate particles around the spanwise axis (x). Since particles settle in a diagonal orientation, ω_x and ω_z show similar behaviour, indicating rotation around the shortest axis (spin). For $El \geq 0.05$, ω_x decays to zero, meaning spinning stops at equilibrium. However, for $El < 0.05$, steady spinning continues, even though the orientation about the y -axis remains stable. Similar to the focusing length in [figure 3\(b\)](#), oblates in low-elasticity fluids ($El < 0.05$) reach a steady orientation faster than in high-elasticity cases ($El \geq 0.05$). Among the latter, alignment occurs notably quicker at $El = 0.1$ than at $El = 0.05$.

In the following subsections, we investigate how yield stress, shear-thinning viscosity and volume fraction of particles change the migration dynamics in EVP fluids.

3.3. Elastoviscoplastic fluid

Now, we shift our focus to EVP carrier fluids, which, in addition to VE stresses, exhibit a yield stress. [Figure 5\(a\)](#) illustrates the final position and orientation of oblate particles in the cross-section of an EVP duct flow, simulated using the Saramito model with elasticity $El = 0.025$, and Bingham numbers varying from 0 to 1. Owing to the lack of sufficient shear stress to yield the material at the duct centre, an unyielded region (plug) forms at the duct core. This plug region is illustrated in the figure for various Bingham numbers, demonstrating its expansion with increasing yield stress. Additionally, [figure 5\(b\)](#) shows

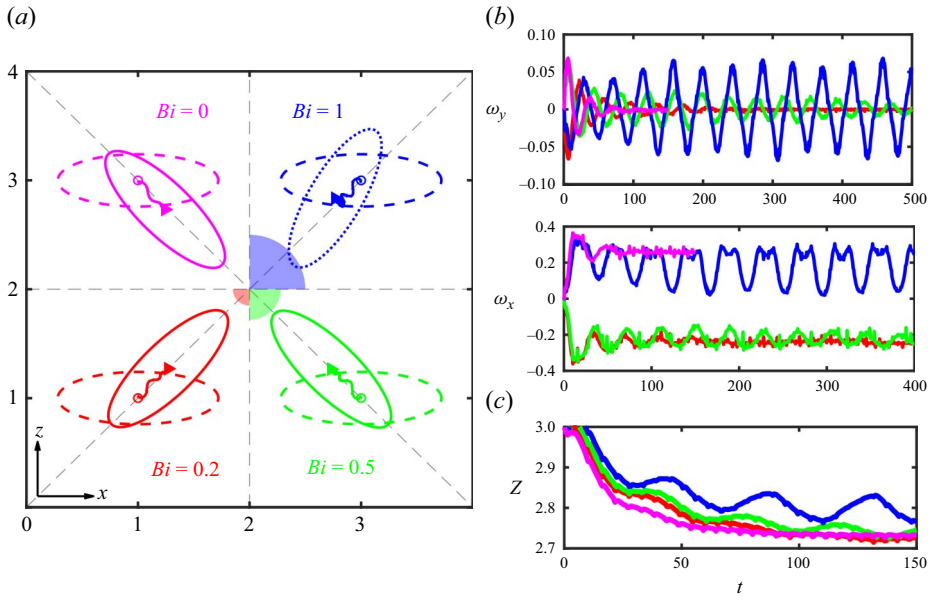


Figure 5. Particle migration in an EVP fluid with $El = 0.025$. (a) Trajectories of oblate particles ($AR = 1/3$) in Saramito duct flows for varying Bingham numbers ($Bi = 0-1$). (b) Streamwise angular velocity (ω_y) and spanwise angular velocity (ω_x) of oblate particles as a function of time. (c) Vertical position of particles over time.

the angular velocities of the particles about the x and y axes, and figure 5(c) presents the particle vertical position over time for each Bingham number.

In the case with $Bi = 0$, the oblate particle migrates towards the duct centre, reaching an equilibrium position situated between the duct walls and the centre, but biased towards the centre. The oblate aligns diagonally within the duct due to the configuration of minimal energy dissipation in shear flows (see § 3.2 for more discussion), and the angular velocity along the streamwise axis (ω_y) approaches zero. Crucially, the values of ω_x remain non-zero, indicating that the oblate undergoes a spinning motion while maintaining its diagonal alignment. Increasing the Bingham number of the suspending fluid up to $Bi = 0.5$ preserves similar steady-state particle behaviour, with final position and orientation consistent with that in VE fluids. However, the particle angular velocities in the y - and x -directions exhibit significantly more pronounced oscillations and tumbling during its migration towards the steady state in the EVP fluid.

At $Bi = 1$, however, the particle angular dynamics undergoes a fundamental change. The oblate particle now exhibits time-dependent rolling and tumbling motions around an equilibrium position situated on the diagonal symmetry line. Consequently, a stable, steady-state orientation or rotation rate cannot be defined at $Bi = 1$ and $El = 0.025$. One representative orientation of the oblate is illustrated with a dotted line in the figure 5(a). The particle angular velocity also displays a distinct behaviour: the angular velocity along the y -axis no longer attains a steady-state value but exhibits quasi-periodic oscillations (see panel (b)). Similarly, the angular velocities along the x -axis display quasi-periodic behaviour. This gyroscopic-like motion can be attributed to the substantial size of the unyielded region (plug) at the duct centre at $Bi = 1$ where the plug comes in contact with the oblate. To clarify, the particle experiences continuous collisions with this plug, which exerts a varying force on the oblate. Analogous to a gyroscope, the oblate responds by precessing and nutating, thereby resisting changes to its angular momentum in the

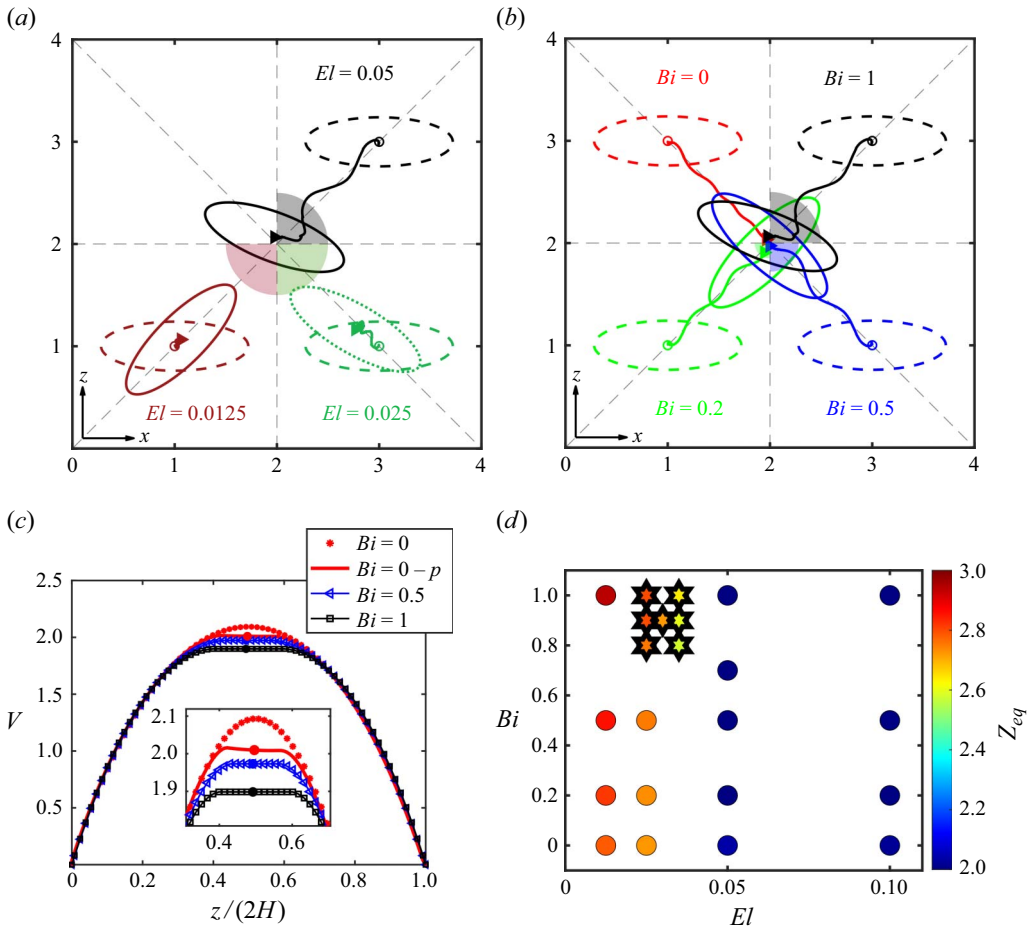


Figure 6. Particle migration in EVP fluids with (a) $Bi = 1$ and varying elasticities $El = 0.01 - 0.05$, (b) trajectories of oblate particles in Saramito duct flows for varying Bingham numbers ($Bi = 0-1$), at $El = 0.05$, (c) streamwise velocity profiles for varying Bi and $El = 0.05$. Far-field profiles (symbols) are compared with profiles across the particle centre at $z/(2H) = 0.5$ (lines); filled circles mark the particle position. The inset provides a magnified view of the central region for clarity. (d) Particle final equilibrium positions as a function of Bi and El . Cases marked with star symbols indicate instances of unsteady angular dynamics.

flow. The magnitude of the angular velocities in this case does not decay over time. Additionally, figure 5(c) shows the vertical position of the particle as a function of time for varying Bingham numbers, indicating that, for $Bi = 0-1$, the particle centre of mass will eventually reach the same equilibrium position. However, as the Bingham number increases, the migration process becomes slower, and the particle trajectory exhibits more pronounced oscillations which delay the migration. Notably, the vertical motion appears to remain periodic at $Bi = 1$.

Turning to the influence of the elasticity number on the observed peculiar dynamics at $Bi = 1$, figure 6(a) presents the final positions and orientations of oblate particles suspended in an EVP fluid with $Bi = 1$, for $El = 0.0125$ to 0.05 . The corresponding particle trajectories, projected onto the duct xz - cross-sectional plane, are also shown. At $El = 0.0125$ and $Bi = 1$, the particle approaches the duct core but remains outside the plug, settling into a diagonal orientation. For $El = 0.025$, the particle interacts with the plug region, exhibiting an unsteady, quasi-periodic angular dynamics (as in figure 5a).

However, at the highest elasticity ($El = 0.05$), the particle migrates further towards the duct centre, penetrating the plug region to reach the duct core. It is noteworthy to note that, although the plug region does not fully encompass the particles, it can nonetheless trap them, preventing rotation and causing the particles to travel at the same velocity as the central plug. In this case, the final orientation of the particle within the plug region is determined by its initial position and orientation, leading to a distribution of potential angles due to variations in the particle entry trajectory. Chaparian *et al.* (2020a) observed centreline migration of a small sphere ($\kappa = 0.1$) under moderate elasticity and $Re = 200$, despite the presence of a plug region. They attributed this to particle rotational inertia inducing local yielding in the surrounding material, enabling deeper plug penetration. Conversely, in our case, the particle remains partially outside the central plug, so the N_1 gradient from the yielded material still actively drives it towards the duct core, resulting in immediate trapping within the plug.

To further examine this effect, figure 6(b) illustrates the steady-state particle configuration in a Saramito fluid, maintained at the highest elasticity value of $El = 0.05$ and for Bingham numbers ranging from $Bi = 0$ to 1. For each Bingham number, the central plug zone is also depicted. In all cases, the particles attain an equilibrium position at the duct core. At a moderate Bingham number ($Bi < 0.5$), the small plug zone yields a dynamics similar to the VE case ($Bi = 0$), with diagonal alignment. In contrast, at higher Bingham numbers ($Bi \geq 0.5$), the larger relative plug size alters the particle final orientation, which now depends on its initial position and orientation at entry to the plug zone. As observed in the figure 6(b), increasing the yield stress intensifies oscillations in the particle xz - trajectory compared with the VE migration. As we will show, this enhanced oscillatory motion delays particle migration towards the duct centre in EVP fluids. Figure 6(c) illustrates the steady streamwise velocity profiles (V) for EVP flows at varying Bi . The unperturbed far-field profiles are shown as solid lines, while symbols represent the perturbed profiles at the particle's cross-section. The final particle positions are indicated by filled circles at the duct centre. In the VE baseline ($Bi = 0$), the far-field profile exhibits a Poiseuille duct flow distribution. In the presence of the particle, the local velocity profile is modified, exhibiting a plateau at the centreline corresponding to the particle's translational velocity. Since the particle equilibrates at the centreline without rotating, the flow disturbance remains localised to its immediate vicinity, and the velocity field recovers rapidly to its far-field state. Notably, the particle lags the flow, as its translational velocity is lower than the unperturbed centreline fluid velocity. This observation is consistent with Li *et al.* (2015), who reported that, at relatively large blockage ratios, central particle migration in Oldroyd-B flows results in a negative slip velocity. In cases with a non-zero Bingham number, a central plug region forms even in the far-field profiles where the shear stress is insufficient to yield the material. Notably, in these cases, the velocity profile across the particle centre identically matches the far-field profile. This occurs because the particle is fully trapped within the central plug; since the relative velocity between the particle and the surrounding medium is zero, the particle induces no additional velocity disturbances in the flow field (see the 3-D visualisation in figure 2e).

Figure 6(d) illustrates the equilibrium position Z_{eq} of oblate particles ($AR = 1/3$) in an EVP duct flow with a confinement ratio of 0.25, as a function of elasticity (El) and Bingham number (Bi). All particles are initially at rest, positioned at $Z_{eq} = 3$ and oriented along the x -axis. The colour of each point denotes the final equilibrium height within the duct cross-section. For $El \geq 0.05$, particles migrate fully to the duct centre (even in the presence of the central plug region), while for $0.012 \leq El < 0.05$, only partial migration to the duct centre occurs, with equilibrium positions between the centre and

the walls (see [figure 6a](#)). An interesting observation is that, at low elasticity numbers, particles remain further away from the centre with increasing Bi , suggesting that yield stress hinders particle migration towards the duct centre. This behaviour can be attributed to two underlying factors. First, the emergence of a central plug region reduces the effective flow area, thereby increasing shear rates and enhancing inertial forces that drive particles towards the walls and corners (Chaparian *et al.* 2020a). Additionally, increasing yield stress in EVP flows promotes particle migration towards the corners by affecting the distribution and gradients of the N_1 , even in the absence of a central plug region as shown by Habibi *et al.* (2025) for spherical particles. As a result, increasing yield stress slightly displaces particles away from the duct centre, even at fixed elasticity. In [figure 6\(d\)](#), cases exhibiting unsteady motion – characterised by persistent tumbling and wobbling – are marked with a hexagonal symbol. In each case, the particle comes in contact with the central plug region, leading to an unsteady rotational dynamics (see [figure 5](#) for details).

To further understand particle migration in EVP fluids, the competing forces on the particle surface must be considered. In these fluids, as in VE media, cross-streamline migration is mainly driven by the gradient of N_1 (Habibi *et al.* 2025). Following Ho & Leal (1976), the elastic lift force on a particle of diameter D scales with the first normal stress difference as: $F_e^p = -(40/3)\pi\rho U_c^2 D_{eq}^2 \kappa El (1 - \beta_s) Z_p$, where Z_p is the dimensionless vertical offset and U_c is the centreline velocity. In contrast, Nizkaya *et al.* (2020) introduced a general form for the inertial lift force acting on an oblate particle as: $F_i^p = \rho C_l a^3 b \dot{\gamma}^2$, where C_l is the lift coefficient. By balancing inertial and elastic forces in EVP fluids, we estimate a critical elasticity number $El_c \approx 0.01$, above which oblate particles with $AR = 1/3$ migrate towards the centreline (see [figure 6a](#)). This threshold includes both partial migration – where the particle is biased towards the centre but remains between the centreline and wall – and complete migration to the duct core. This value aligns with previous findings for spherical particles in VE (Li *et al.* 2015) and EVP fluids (Habibi *et al.* 2025) and for oblates with $AR = 1/2$ in VE media (Li *et al.* 2024). As the elasticity of the fluid increases, the resulting lift force strengthens, allowing the particles to overcome the yield-stress barrier and enter the plug region. Our simulations for $Bi = 0-1$ show that an elasticity number of $El = 0.05$ is sufficient to drive particles fully into the duct core (complete migration). Additional effects of particle shape in EVP fluids are discussed in [Appendix B](#).

3.4. Effect of shear thinning in elastoviscoplastic fluids

Up to this point, we have examined the effects of viscoelasticity and yield stress on the oblate particle migration. However, many VE and EVP materials in nature and industries exhibit shear-thinning behaviour. To this end, we employ the Saramito–Giesekus model to simulate the carrier fluid, as it captures viscoelasticity, yield stress and shear-thinning effects within a unified framework (see § 2.1). It also accounts for weak secondary flows in a duct flow (Li *et al.* 2015; Habibi *et al.* 2025).

[Figure 7\(a\)](#) illustrates particle migration and orientation in an EVP fluid across a range of shear-thinning plastic viscosities, from $\alpha = 0$ (no shear-thinning viscosity) to 0.3 (highest shear-thinning viscosity), with an elasticity of 0.05 and a Bingham number of 1. The central plug region for each fluid is also depicted. Notably, the introduction of shear thinning significantly expands the plug size compared with the case with constant plastic viscosity ($\alpha = 0$). In the non-shear-thinning EVP case ($\alpha = 0$), as described before, the particles migrate to the centre of the duct. However, in the shear-thinning cases $\alpha > 0$, the particles exhibit a surprising behaviour, moving away from the duct centre (plug zone) towards the walls and settling in an equilibrium position between the centre and

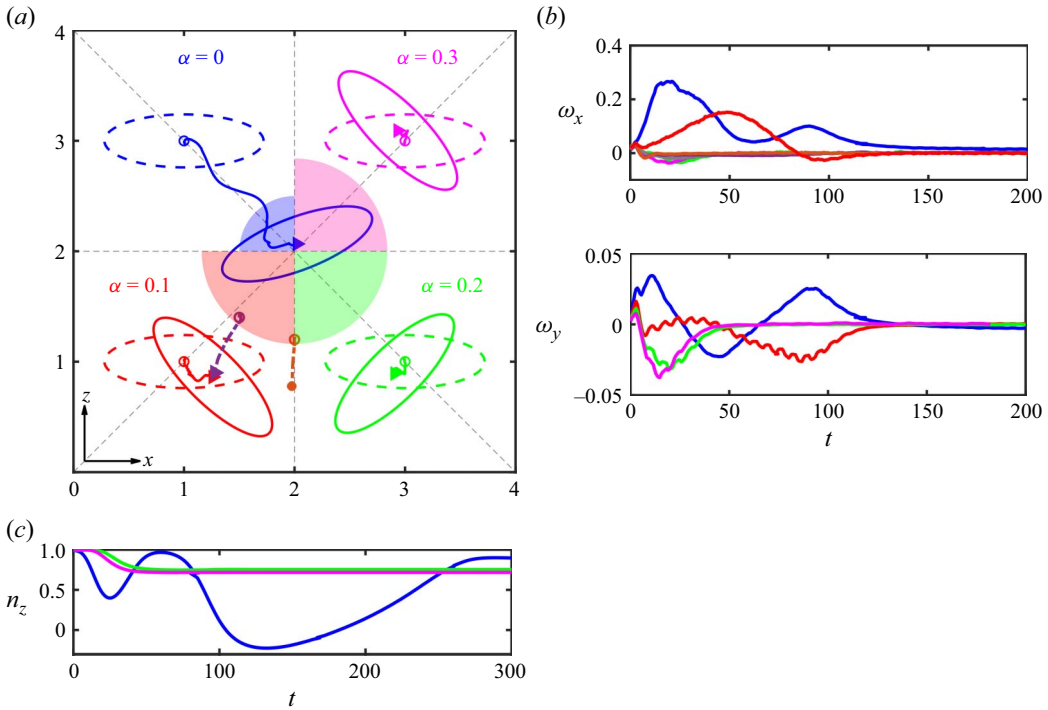


Figure 7. Effect of shear-thinning viscosity in oblate migration in an EVP fluid with $El = 0.05$ and varying mobility parameters (α). (a) Trajectories of oblate particles suspended in fluids with $\alpha = 0 - 0.3$. In the case of $\alpha = 0.1$, particles are released from various initial positions. (b) Temporal evolution of the spanwise (ω_x) and streamwise (ω_y) angular velocities of oblates. (c) Time evolution of the z component of the orientation axis of the oblate particle.

the corners, while orienting perpendicular to the diagonal symmetry lines. We further simulated two additional cases with varying initial positions within the quadrant of $\alpha = 0.1$. The results indicate that even when released near the central plug, the particle migrates away from the duct centre and equilibrates at the same lateral position between the centre and the walls. Due to symmetry, a particle released exactly on the symmetry line ($x = 2$) follows a straight trajectory toward the duct walls while orienting itself perpendicular to the z -axis. Migration of oblate particles in shear-thinning fluids is notably rapid; within fewer than 100 non-dimensional time units for $\alpha = 0.1$ and 50 time units for $\alpha = 0.2$ and 0.3 , the particle angular velocity decays to zero (see figure 7b), and it adopts a stable, perpendicular orientation. In contrast to Newtonian, VE and Saramito-type fluids – where particles undergo sustained Jeffery-like oscillations before settling – the shear-thinning case features only a single oscillation prior to reaching equilibrium. Notably, unlike in Saramito fluids, where particles tend to align along the duct diagonals while spinning, in Saramito–Giesekus fluids they remain perpendicular to them, exhibiting neither spin nor tumbling motion. Panel (c) shows the time evolution of the z -component of the orientation axis for the oblate particle. We compare the case of $\alpha = 0$ with cases involving shear thinning. The colour coding in this plot is consistent with that used in panel (a). As observed, the particle reaches a stable orientation significantly faster ($t \approx 50$) in the presence of shear-thinning plastic viscosity. In contrast, for the $\alpha = 0$, the particle migrates towards the duct centre and penetrates the plug region, requiring a much longer time to achieve a steady-state orientation ($t \approx 280$).

Habibi *et al.* (2025) analysed the physical mechanism governing the behaviour of spherical particles in Saramito–Giesekus fluids. Their findings show that the shear-thinning effect – introduced by the nonlinear term $Wi\alpha/(1 - \beta_s)(\boldsymbol{\tau}^p \cdot \boldsymbol{\tau}^p)$ – reduces elastic stresses and diminishes centre-directed migration. Consequently, particles preferentially migrate towards the walls and corners when $\alpha > 0.1$. Additionally, shear thinning lowers the apparent viscosity at high shear rates, steepening velocity gradients near the walls and flattening the velocity profile. This amplifies the shear-gradient lift force – scaling as $F_L \sim \rho U^2 a^6 / H^4$ (Di Carlo *et al.* 2009) – further promoting wall-directed migration (Villone *et al.* 2013; Li *et al.* 2015; Habibi *et al.* 2025). As a result of these two mechanisms, particles in Saramito–Giesekus fluids migrate towards the duct walls rather than the centre, in contrast to the Saramito case.

A novel observation in the present study is the stable orientation of oblate particles perpendicular to the duct diagonals in the Saramito–Giesekus suspension. Orienting the side with the smaller surface area in the streamwise direction reduces the surface exposed to the flow and is therefore energetically favourable; however, this does not explain why the particle avoids diagonal alignment seen in VE and Saramito EVP cases. However, strong elastic and repulsive forces from adjacent walls (see figure 3*d*) inhibit diagonal orientations with particle tips directed into corners. Consequently, particles stabilise in orientations perpendicular to the diagonals, balancing minimal flow resistance with wall avoidance.

To examine the influence of yield stress on the orientation of oblate particles in shear-thinning fluids, we vary Bi from 0 (purely VE) to 1, as shown in figure 8(*a*). In the VE and weak yield-stress cases ($Bi < 1$), particles partially migrate towards the duct centre, while at $Bi = 1$, they slightly shift towards the duct corners. This indicates that although shear-thinning effects tend to drive particles towards the corners (through weakening of the elastic effects), the distinct orientation perpendicular to the duct diagonals requires a sufficiently large central plug region. Figure 8(*b*) shows the vertical position of the particle over time, revealing that increasing yield stress pushes the equilibrium position further from the centre, suggesting a stronger influence of inertia. While particles reach positional equilibrium quickly in both VE and EVP fluids, at $Bi < 1$ their angular motion exhibits long oscillations, gradually damping to zero. In contrast, the $Bi = 1$ case rapidly reaches zero angular velocity within 50 time units. The perpendicular orientation of the oblate relative to the duct diagonals remains stable, as it aligns with the axis of maximum moment of inertia towards the walls, and the shear-stress asymmetry at its tips is insufficient to induce rotation. Conversely, when the oblate is oriented along a diagonal (as in cases with $Bi < 1$), a pronounced stress imbalance develops across its sides, leading to sustained particle spin at equilibrium. To further investigate this phenomenon, panel (*c*) presents the streamwise velocity profiles of the Saramito–Giesekus fluids across a range of Bi . As observed, the spatial extent of the plug region expands significantly with increasing yield stress. Since the bulk velocity V_b is held constant, the reduction of the centreline velocity at higher Bi must be compensated by a lateral expansion of the 3-D velocity paraboloid. This redistribution of the flow field steepens the velocity gradients in the near-wall regions for flows with higher Bi . This effect is captured in the inset, where a magnified view of the velocity profile at the duct corner is shown; here, the dashed lines representing the wall velocity tangents for $Bi = 0$ and $Bi = 1$ clearly illustrate the sharpening of the gradient. As discussed earlier, these intensified velocity gradients enhance the inertial lift forces – which scale with the local shear rate (Ho & Leal 1974; Li *et al.* 2015) – thereby driving the particles further away from the duct centre towards the walls.

To conclude this subsection, figure 8(*d*) illustrates the equilibrium position (Z_{eq}) of oblate particles ($AR = 1/3$) in Saramito–Giesekus duct flows with a confinement ratio of

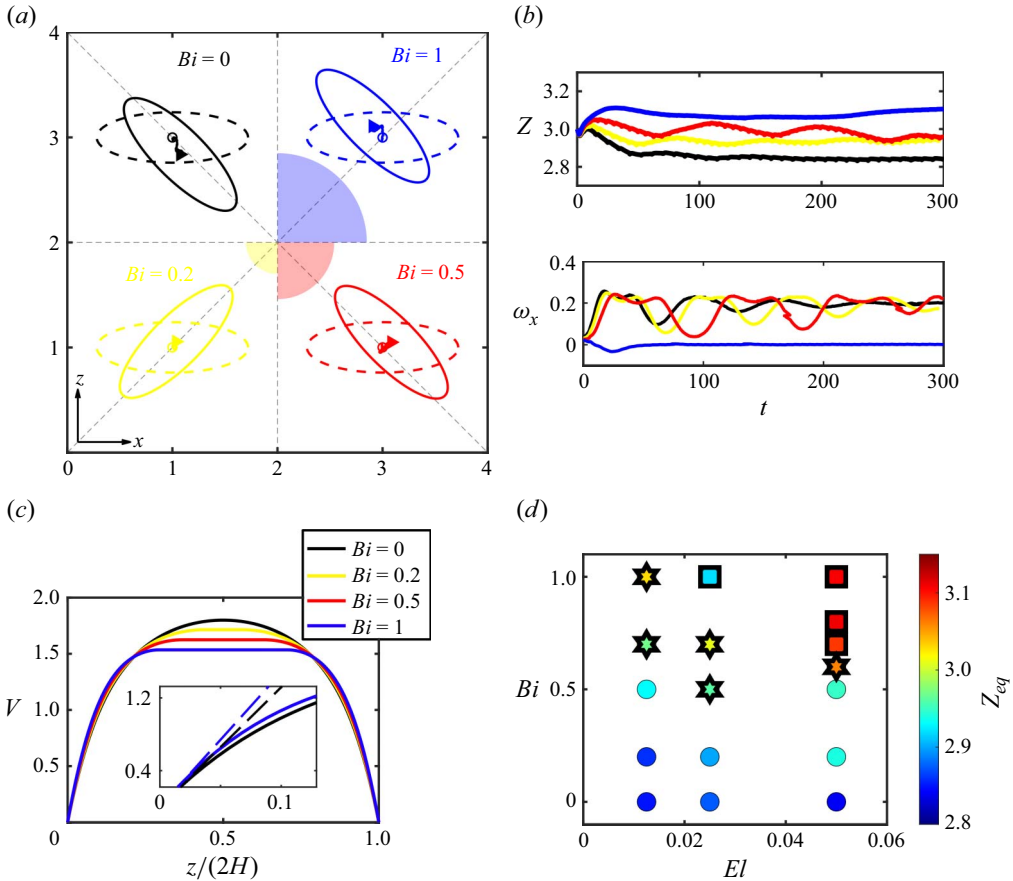


Figure 8. Effect of Bingham number on oblate migration in an EVP fluid with $El = 0.05$ and $\alpha = 0.2$. (a) Trajectories of oblate particles suspended in fluids with $Bi = 0 - 1$, and (b) time evolution of the particle vertical position and the spanwise angular velocity (ω_x). (c) Streamwise mean velocity profiles of Saramito–Giesekus fluids for various Bi . The inset provides a magnified view of the near-wall region, where dashed lines represent the velocity tangents. (d) Mapping of particle equilibrium positions and orientations in the $BiEl$ -plane for Saramito–Giesekus fluids with $\alpha = 0.2$. The vertical equilibrium position is represented by the colour bar (right). Orientation modes are distinguished by symbols: squares for normal-to-diagonal alignment, circles for diagonal alignment and stars for cases exhibiting an unsteady angular dynamics.

0.25, plotted as a function of El and Bi for $\alpha = 0.2$. In these simulations, all particles were released from rest at $Z = 3$ with an initial orientation normal to the z -axis. The data points are colour coded to represent the final equilibrium height within the duct cross-section. Across the entire range of elasticity values investigated, the particles migrate away from the walls towards the duct corners. This lateral migration is further enhanced by increasing elasticity, which drives the particles towards the corner regions – the areas of minimum shear rate and elastic stress. This observation aligns with the findings of Habibi *et al.* (2025), who demonstrated that increased elasticity in Saramito–Giesekus fluids laden with spherical particles promotes migration towards the duct corners. Notably, the particles maintain a greater lateral distance from the duct centre with increasing Bi . This suggests that in Saramito–Giesekus fluids – analogous to the behaviour observed in Saramito fluids – the yield stress effectively promotes migration towards the corners by augmenting the inertial lift forces. The angular dynamics of the particles is also mapped in the same figure.

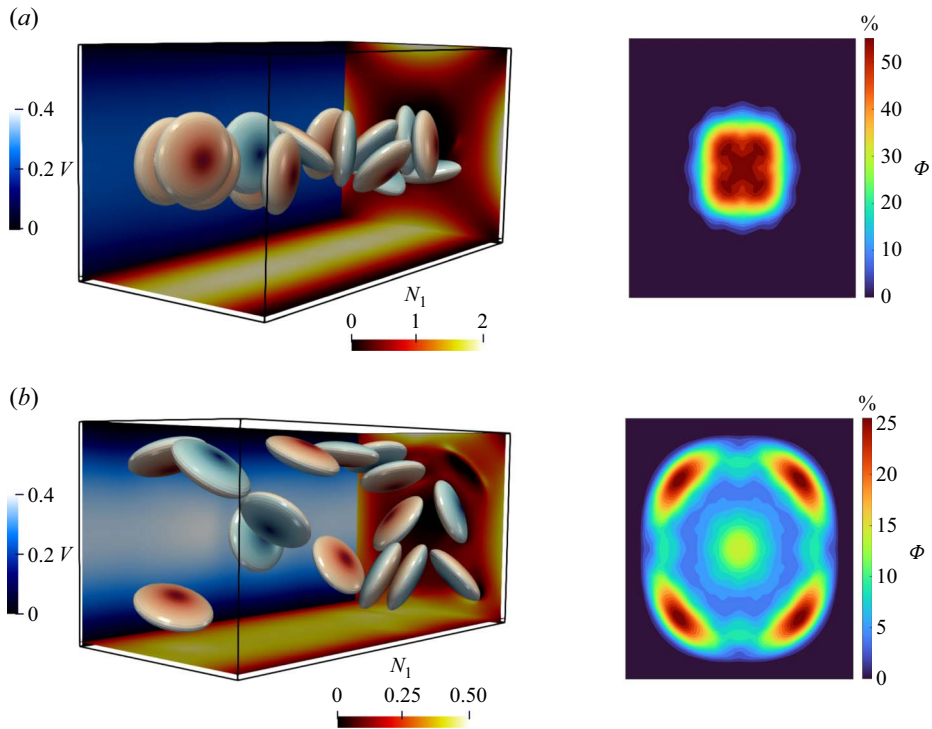


Figure 9. Instantaneous snapshots of the flow field (left column) and mean particle concentration $\Phi(x, z)$ (right column) across the duct cross-section are shown for (a) the Saramito EVP fluid with $El = 0.05$, $Bi = 1$, and (b) the Saramito–Giesekus fluid with $El = 0.05$, $Bi = 1$ and $\alpha = 0.2$. In all cases, the solid volume fraction is $\phi = 6\%$ and the Reynolds number is $Re = 20$. The 3-D contours in the flow field snapshots depict the first normal stress difference (N_1) and the streamwise velocity (v).

Depending on the specific combination of El and Bi , the particles either align with the duct diagonals (denoted by circular symbols) or orient themselves normal to the diagonals (square symbols). At low Bi , the particles favour a diagonal orientation; this represents the most energetically favourable state as it minimises drag and maximises the distance from the confining duct walls (Lashgari *et al.* 2017). At intermediate Bi , the particles exhibit unsteady angular behaviour, characterised by persistent tumbling and wobbling, similar to regimes observed in Saramito fluids (cf. figure 5a). In these cases, the particle is situated in close proximity to, or in direct contact with, the central plug region; the resulting contact torque with the rigid plug leads to this unsteady rotational dynamics. With a further increase in yield stress, this transient unsteady regime eventually transitions into a stable state where the particle remains oriented normal to the diagonal.

3.5. Collective behaviour of oblate particles

In this subsection, we examine the migration and orientation behaviour of suspensions of oblate particles and compare this dynamics with those of spherical particles. We first investigate a suspension of oblate particles with an aspect ratio of $1/3$, at a solid volume fraction of $\phi = 6\%$, flowing through a duct characterised by a blockage ratio $\kappa = 0.25$. Figure 9 displays instantaneous three-dimensional snapshots of the flow field and particle distribution at statistically steady states for two carrier fluids: a Saramito fluid (figure 9a) and a shear-thinning Saramito–Giesekus fluid (figure 9b). Each snapshot illustrates the distributions of the first normal stress difference (N_1) and the streamwise

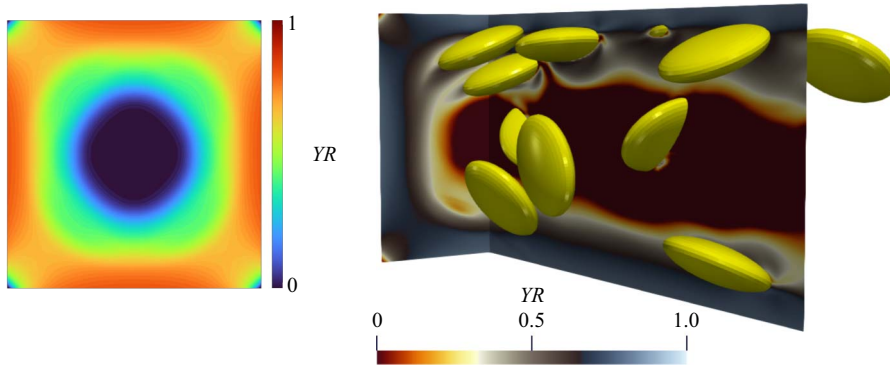


Figure 10. Time and spatially averaged distribution of yielded and unyielded regions (YR) in a suspension of oblate particles within an EVP fluid modelled using the Saramito–Giesekus formulation, together with an instantaneous 3-D view of unyielded regions ($YR = 0$) and particle positions. The YR map shows the yielding probability at each location, where $YR = 0$ indicates a solid-like behaviour and $YR = 1$ indicates a fully yielded region.

velocity (v) on their respective planes. Complementing these visualisations, we present the probability distribution function of the concentration, $\Phi(x, z)$, representing the time and spatially averaged solid phase distribution across the duct cross-section. All simulations are conducted at a Reynolds number $Re = 20$. For the EVP model, the elasticity number is fixed at $El = 0.05$ and the Bingham number at $Bi = 1$. It is worth emphasising that the Saramito model assumes a constant polymer viscosity ($\alpha = 0$), while the Saramito–Giesekus model incorporates shear-thinning behaviour through a non-zero mobility factor ($\alpha = 0.2$); recall the governing equations in § 2.1.

In the Saramito carrier fluid, particles migrate towards the duct centre, penetrating the central plug region and forming a concentrated cluster of oblate particles. Within this cluster, the particles exhibit a broad range of angular orientations without clear preferential alignment. This contrasts with the single-particle simulations presented previously in this work, where an isolated particle adopts a stable diagonal orientation at the centreline. The disparity is attributed to the collective dynamics, where particle–particle interactions disrupt the alignment seen in isolated cases and give rise to a wider distribution of orientations.

In contrast to the Saramito suspension, the Saramito–Giesekus fluid drives particles towards the walls and corners of the duct, leading to the formation of distinct chains of oblate particles with preferred orientations nearly perpendicular to the diagonal, as in the single-particle case. While the majority of particles migrate from the duct centre towards the walls, a subset remains near the centre. To explain this, we examine the unyielded regions of the flow shown in figure 10, which includes a 3-D snapshot of the unyielded zones together with the time-averaged yielded region (YR) across the duct cross-section. The YR map represents the probability of the material being yielded at each location, with $YR = 0$ indicating fully unyielded, solid-like behaviour while with $YR = 1$ represents fully yielded region. At the duct centre, where shear stress is minimal, the material remains unyielded, forming a central plug that moves at the maximum flow velocity. As illustrated in the figure, while the majority of particles are driven towards the corners, those initially located near the centre can become entrained within the plug. These particles remain effectively stationary relative to the plug and are passively advected at the plug velocity. Trapping particles were observed also in the single-particle case in previous sections, but only for the Saramito fluid.

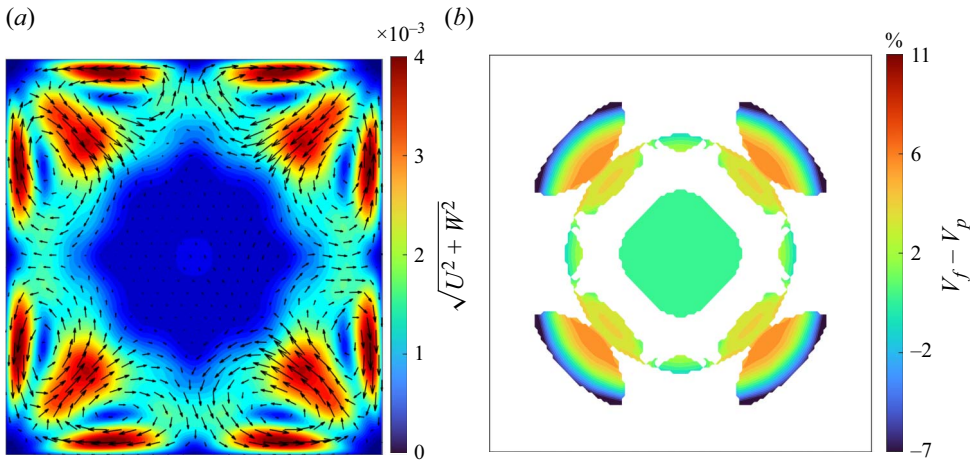


Figure 11. (a) Secondary flows in EVP suspension with $Bi = 1$, $El = 0.05$ and $\alpha = 0.2$. For both cases $\phi = 6\%$ and $Re = 20$. (b) The difference between the time-averaged velocities of the fluid and particles, normalised by the bulk flow velocity. White regions indicate locations where no particles are present.

Another notable phenomenon observed in the Saramito–Giesekus simulations is the emergence of secondary flows, attributed to the combined effects of the second normal stress difference (N_2) and the non-circular duct geometry (Yue, Dooley & Feng 2008). The presence of particles further amplifies these flows by introducing disturbances into the velocity field. As shown in figure 11(a), the secondary flow field in the EVP suspension at a particle volume fraction of $\phi = 6\%$ consists of eight vortical structures. The peak magnitude of these secondary flows reaches approximately 4×10^{-3} . No secondary flows are observed at the duct centre, as this region is occupied by the unyielded plug, where the EVP material behaves as a solid and thus cannot support shear-driven vortical motion. In Saramito–Giesekus flows, the secondary flow magnitude exceeds the lateral migration velocity of the particles ($O(10^{-3})$), thereby driving the particles further towards the duct corners.

In addition to secondary flows, figure 11(b) presents the time-averaged streamwise velocity profiles of the percentage difference between the fluid and oblate particle velocities ($V_f - V_p$), relative to the bulk velocity in the EVP suspension, plotted across the duct section. As shown, the particle velocity in the duct core matches that of the plug (zero velocity difference), confirming that particles enclosed within the plug are carried along with it. Further away from the centreline, however, particle average velocities slightly lag behind the fluid (approximately 11% of the bulk velocity), primarily due to particle inertia. However, there exists a narrow region where the fluid velocity falls below that of the particles.

Finally, we compare the migration behaviour of oblate and spherical particles. Figure 12 depicts 3-D snapshots of suspensions containing 6% volume fraction of either oblate or spherical particles in a Saramito–Giesekus duct flow. All rheological parameters are identical between the two cases, with particle shape being the only difference. To further illustrate particle distribution, the time and spatially averaged concentration $\Phi(y, z)$ is also presented for the oblate particles with $AR = 1/3$ and $1/2$ and the spherical suspensions. This quantity represents the mean solid phase concentration across the duct cross-section. In all cases, particles migrate from the duct centre towards the corners. Spherical particles settle at the corners, while oblate particles reach equilibrium slightly away from them, collectively forcing a small number of particles to be trapped in the centre. Among the

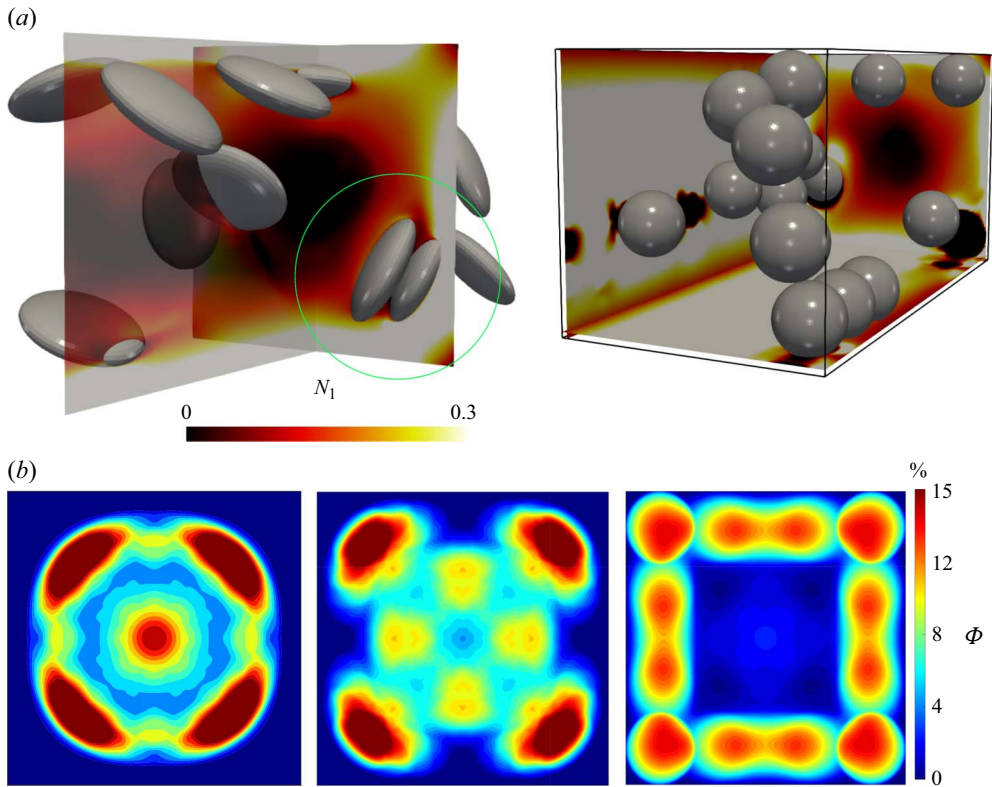


Figure 12. Effect of particle shape on migration in an EVP medium: (a) instantaneous snapshots of particle distributions and flow fields in Saramito–Giesekus fluids for oblates with $AR = 1/3$ and spheres, with planes indicating N_1 values; (b) mean particle concentration profiles for aspect ratios $AR = 1/3, 1/2$ and 1.

oblate cases, particles with an aspect ratio of $1/3$ remain farther from the wall compared with those with $AR = 1/2$. This difference arises from the higher shear gradients at the oblate tips, which enhance wall repulsion and the first normal stress difference (note the green circle in figure 12a). These increased forces, particularly near the sharper tips of oblates, prevent them from reaching the corners. Due to their anisotropic shape and larger effective surface area when aligned perpendicular to the diagonals, oblates experience stronger wall-induced repulsion. This interaction, especially in confined geometries, outweighs migration forces and causes oblates to stabilise near – but not at – the corners. Conversely, isotropic spheres experience symmetric wall forces and, under strong VE and shear-thinning effects in the Saramito–Giesekus fluid, can settle stably at the corners where shear and elastic force are minimal (Habibi *et al.* 2025). This shape-dependent behaviour is particularly relevant for microfluidics applications, as it enables particle separation based on shape and aspect ratio. Such an approach can complement existing sorting techniques, including inertial microfluidics (Masaeli *et al.* 2012).

4. Concluding remarks

A flowing suspension of particles in EVP fluids presents a complex dynamics due to the interplay of multiple mechanisms influenced by both particle geometry and the rheological properties of the fluid. Given the importance of EVP fluids in both natural and industrial contexts, their detailed study is essential. To this end, we performed 3-D, interface-resolved DNS to investigate the dynamics of rigid spheroidal particles in EVP duct flows.

In all cases, inertial effects were included. We employed the Saramito and Saramito–Giesekus models to capture the EVP behaviour of the fluid, resolving particle–fluid interactions using the IBM, along with lubrication corrections and a soft-sphere collision model to account for inter-particle and particle–wall interactions.

We initially examined the migration of single spheroidal particles in VE fluids, then extended our study to incorporate yield-stress effects characteristic of EVP fluids. We further analysed suspensions of oblate particles and identified key differences between individual and collective behaviours. The main findings are summarised below.

- (i) In Saramito-modelled EVP fluids, particles migrate towards the duct centre when the elasticity number exceeds 0.01, consistent with VE cases, due to the gradient of the first normal stress difference (N_1). For elasticity numbers above 0.05, particles are able to fully enter the plug region, moving at the same velocity as the plug and without rotation relative to it. We also demonstrated that increasing yield stress at fixed elasticity causes oblates to shift towards the duct walls and corners, in contrast to previous findings about spherical particles.
- (ii) The angular dynamics of particles is strongly influenced by both elasticity and yield stress. At moderate elasticity ($El \simeq 0.025$) and high yield stress ($Bi \geq 1$), the plug region becomes comparable in size to the particle, resulting in partial contact and inducing gyroscopic motion to the particles. As a result, particles interacting with the plug exhibit unsteady, periodic spinning and tumbling. In contrast, particles that fully enter the plug ($El \geq 0.05$) adopt its velocity and cease rotation, with their final orientation strongly influenced by their entry angle, determined by their initial position and orientation. At lower elasticity ($El < 0.02$), particles align with the duct diagonals between the centre and corners without interacting with the plug, resembling VE behaviour.
- (iii) In Saramito–Giesekus fluids, particles tend to migrate away from the centre towards the corners due to weakened elastic forces and enhanced wall-directed inertial effects from the shear-thinning viscosity. Nevertheless, for sufficiently large plug regions ($Bi \geq 1$), oblate particles stay away from the corners and align perpendicularly to the duct diagonals. In such cases, particles rapidly reach a steady state with negligible angular velocities, deviating from classical Jeffery orbits. When the plug is smaller, particles move towards the wall along a diagonal trajectory and spin, but do not exhibit tumbling.
- (iv) The dynamics of dilute and semi-dilute suspensions largely mirrors that of single particles. In Saramito fluids, particles accumulate in the plug region and display a wide range of orientations due to collision-induced variability. In Saramito–Giesekus fluids, particles form trains near duct corners, aligned perpendicularly to the diagonals and moving slightly faster than the local fluid. Secondary flows also emerge in Saramito–Giesekus cases, with magnitudes comparable to the particles lateral migration velocity, further promoting their migration towards the corners.
- (v) Finally, we compared suspensions of oblate particles (aspect ratios 1/3 and 1/2) with spherical particles ($AR = 1$). Spherical particles accumulate at the duct corners, overcoming wall-repulsion forces. In contrast, oblate particles experience stronger wall-repulsion and elastic forces, causing them to settle slightly away from the corners. This distance increases with decreasing aspect ratio (i.e. for more flattened particles). These shape-dependent interactions suggest a promising route for particle separation in microfluidics applications, where the complex flow behaviour of EVP fluids can be harnessed to sort particles by shape.

Acknowledgements. The authors acknowledge the computer time provided by SNIC and NAISS (National Academic Infrastructure for Super-computing in Sweden).

Funding. This project has received funding from the European Union's Horizon 2020 research and innovation program under the Marie Skłodowska-Curie grant agreement No. 955605 YIELDGAP. We gratefully acknowledge the support of European Research Council through Starting Grant MUCUS (Grant No. ERC-StG-2019-852529).

Declaration of interests. The authors report no conflicts of interest.

Appendix A. Code validation

A.1. Resolution and box size studies

The numerical solver used in this study has been successfully applied and validated in various configurations, including the sedimentation of rigid particles in EVP media (Sarabian *et al.* 2020), the dynamics of soft particles and droplets in EVP flows (Izbassarov *et al.* 2018; Izbassarov & Tammsisola 2020), EVP flow through porous structures (De Vita *et al.* 2018; Chaparian *et al.* 2020*b*) and turbulent EVP flows (Rosti *et al.* 2018; Izbassarov *et al.* 2021). Additionally, Habibi *et al.* (2025) demonstrated that our numerical results for spherical particle suspensions in EVP duct flows exhibit excellent agreement with existing experimental velocity profiles for finite-size particles in Carbopol duct flows.

For the sake of completeness, we present four additional validation tests. The first assesses the sensitivity of the results to domain size and grid resolution. The baseline simulation is conducted in a square duct of size $2h \times 6h \times 2h$, discretised using a $160 \times 480 \times 160$ grid, corresponding to a resolution of 32 grid points per particle diameter. To evaluate the influence of streamwise periodicity on the simulation results, we extend the domain length to $8h$ while keeping the grid resolution unchanged, resulting in a $160 \times 640 \times 160$ mesh (denoted as 'Long'). We also consider a high-resolution case (referred to as 'Res40') with the same domain size but a refined grid of $200 \times 600 \times 200$, corresponding to 40 Eulerian grid points per particle diameter and 5036 Lagrangian markers on the particle interface.

In all configurations, we track a particle ($(2h)/D_p = 4$) in a Saramito fluid at $Re = 20$, $Wi = 1$, and $Bi = 1$. We observe that the particles, initially positioned at $Z_p, X_p = 3$, gradually migrate towards the duct centreline. The results, shown in figure 13, demonstrate a great agreement in lateral velocity, angular velocity, migration trajectory and equilibrium position of particles across all test cases. This consistency supports the use of the reference case ('Res32') for the main simulations.

A.2. Immersed boundary method solver validation

The second validation case assesses the angular velocity of a spheroidal particle in a Couette flow, comparing simulation results with Jeffery's analytical solution (Jeffery 1922) for aspect ratios $AR = 1/3$ and $1/2$. The particles are neutrally buoyant suspended in the middle of a plane Couette flow at particle Reynolds number $Re_p = 0.1$. Here, Re_p is defined by shear rate $\dot{\gamma}$ and the equivalent particle diameter D_{eq} as $Re_p = \rho \dot{\gamma} D_{eq}^2 / \mu$.

Simulations are conducted in a cubic domain of size $10D_{eq} \times 10D_{eq} \times 10D_{eq}$ using resolution of 32 grid points per D_{eq} . Periodic boundary conditions are applied in the directions perpendicular to the velocity gradient, while no-slip and no-penetration conditions are enforced along the wall-normal direction. The initial particle orientation is aligned with the x -direction, with no initial angular velocity. As expected, the particles exhibit periodic tumbling motion around the spanwise axis, which is normal to the shear

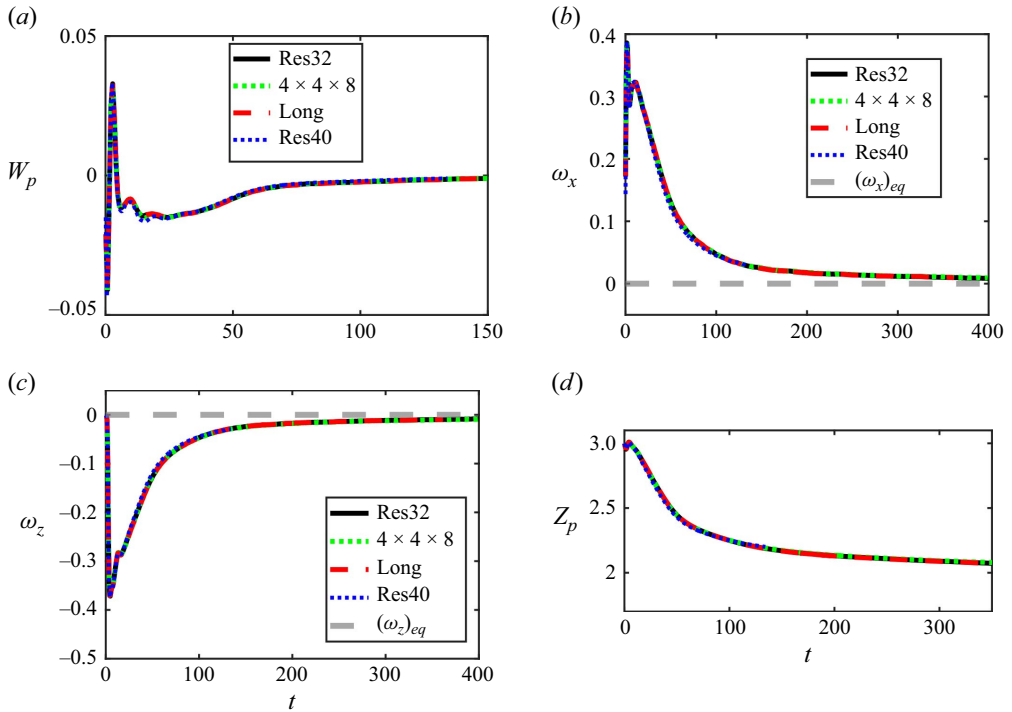


Figure 13. Comparison of the temporal variation of (a) vertical migration velocity (W_p), (b) angular velocity around x-axis, (c) angular velocity around z-axis and (d) vertical position of the particle (Z_p). Simulations correspond to Saramito model with $Re = 20$, $Wi = 1$, $Bi = 1$ and $\kappa = 0.25$.

plane. The results, presented in figure 14(a), show excellent agreement between our DNS simulations and Jeffery’s analytical solution.

To further validate the IBM and VE solvers, we benchmark our numerical method against a canonical problem involving the angular velocity of a neutrally buoyant sphere suspended at the centre of a 3-D Couette flow of an Oldroyd-B fluid. Experimental measurements by Snijkers *et al.* (2011) and DNS by Goyal & Derksen (2012) characterised the particle rotation as a function of the Weissenberg number, $Wi = \lambda\dot{\gamma}$, varying from 0 to 2. The Couette cell has dimensions $4R \times 8R \times 8R$ and is discretised with 24 grid points per particle diameter. Opposing wall velocities $\pm U$ generate a shear rate $\dot{\gamma} = 2U/8R$, with periodic boundary conditions applied in the remaining directions. The particle experiences rotation solely about the z-axis, and the particle Reynolds number is fixed at 0.025 (creeping flow regime).

As shown in figure 14(b), our results (shown by ‘DNS’ label) closely match the experimental data, capturing the observed reduction in angular velocity with increasing Wi , consistent with the known effect of elasticity in suppressing particle rotation.

A.3. EVP solver validation

In this subsection, we assess the accuracy of the EVP solver by considering planar Couette flow of a Saramito–Giesekus fluid. The material is initially at rest ($t = 0$), after which a constant shear rate $\dot{\gamma}_0$ is applied. The Weissenberg and Bingham numbers are defined as $Wi = \lambda\dot{\gamma}_0$ and $Bi = \tau_0/(\mu\dot{\gamma}_0)$, respectively. In 2-D simple shear flow, the tensorial form of the constitutive equation (see (2.3)) reduces to the following set of coupled ordinary

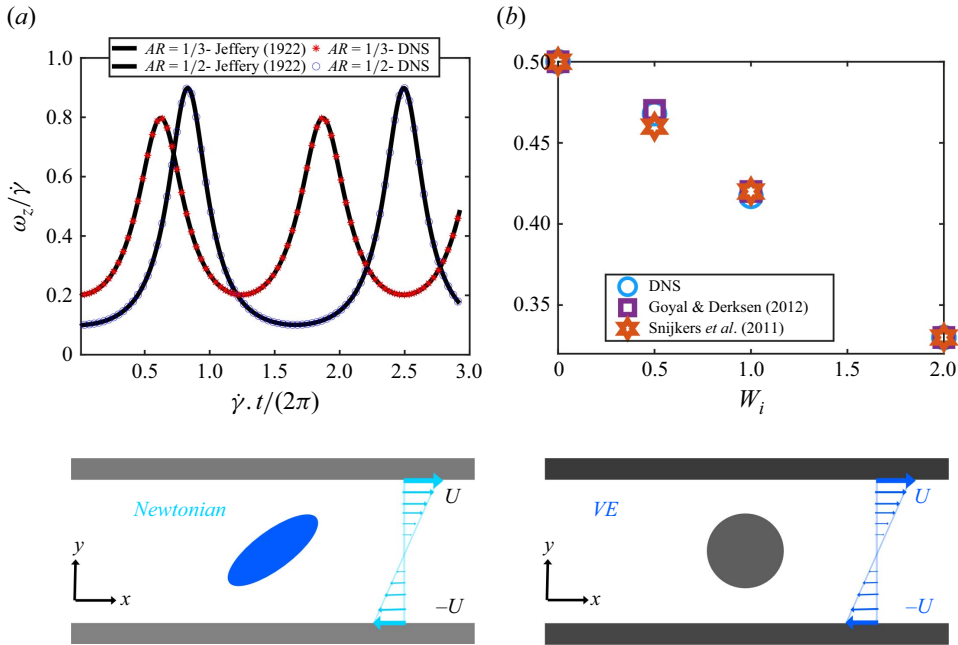


Figure 14. (a) Angular velocity of ellipsoids with aspect ratios $AR = 1/2$ and $1/3$. The DNS results from the present study are compared with Jeffery’s analytical solution (Jeffery 1922). The particle Reynolds number is $Re_p = 0.1$. A schematic of an oblate particle suspended in Couette flow is shown at the bottom of panel (a). (b) Angular velocity of a sphere in a VE Couette flow as a function of the Weissenberg number (Wi), with $Re_p = 0.025$. Blue circles (labelled ‘DNS’) denote results from the present numerical solver. The bottom of panel (b) displays a schematic of a sphere suspended in VE Couette flow.

differential equations:

$$Wi \frac{d\tau_{xx}}{dt} - 2Wi \tau_{xy} + F \left(\tau_{xx} + \frac{Wi \alpha}{(1 - \beta_s)} (\tau_{xx}^2 + \tau_{xy}^2) \right) = 0, \quad (A1)$$

$$Wi \frac{d\tau_{yy}}{dt} + F \left(\tau_{yy} + \frac{Wi \alpha}{(1 - \beta_s)} (\tau_{xx} \tau_{xy} + \tau_{xy} \tau_{yy}) \right) = 0, \quad (A2)$$

$$Wi \frac{d\tau_{xy}}{dt} - Wi \tau_{yy} + F \left(\tau_{xy} + \frac{Wi \alpha}{(1 - \beta_s)} (\tau_{xy}^2 + \tau_{yy}^2) \right) = 1 - \beta_s. \quad (A3)$$

Here, $F = \max(0, |\boldsymbol{\tau}_d| - Bi/|\boldsymbol{\tau}_d|)$ and $|\boldsymbol{\tau}_d|^2 = 1/2(\boldsymbol{\tau}_d : \boldsymbol{\tau}_d)$. The initial condition for all the stress components is fixed at zero ($\boldsymbol{\tau}(t=0) = \mathbf{0}$). The above equations are solved numerically for the case of $Re = 0.05$, $Bi = 0.2$, $Wi = 1$, $\beta_s = 1/9$ and $\alpha = 0.2$. Figure 15 illustrates the temporal evolution of the shear stress (τ_{xy}) and the first normal stress difference (N_1) obtained by our numerical code in comparison with the semi-analytical solution obtained using the framework in Saramito (2007, 2009). The shear stress initially rises, leading to a tiny overshoot, and then it falls until it eventually reaches a steady value. It is noteworthy that the Saramito model captures the stress overshoot as it is a phenomenon that is observed in the startup shear of polymeric liquids. The reader can find more details in Schweizer & Xie (2018) and Tseng (2021) who discuss the origin of the stress overshoot in the startup Couette flow of polymeric liquids from the perspective of the polymer microstructure, and how constitutive equations may capture it.

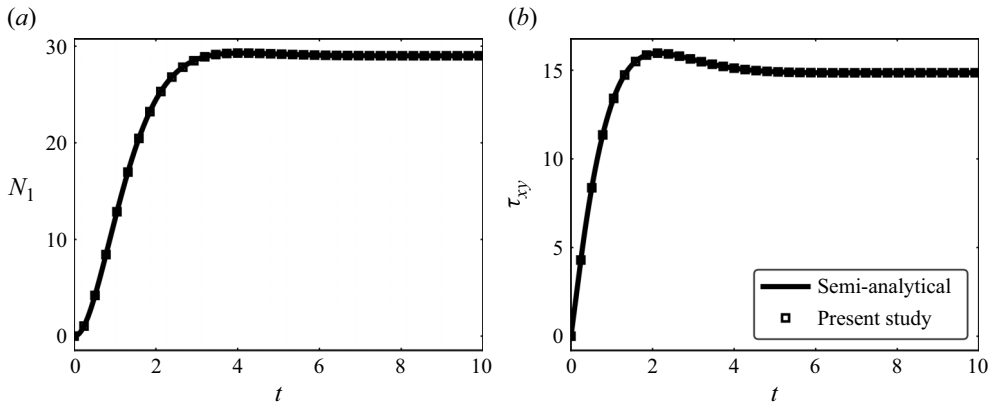


Figure 15. Evolution of (a) the first normal stress difference and (b) shear stress in time for a planar Couette flow with $Re = 0.05$, $Bi = 0.2$, $Wi = 1$ and $\alpha = 0.2$. The solid line represents the semi-analytical solution, while the square symbols are the result of the present numerical code.

A.4. Migration of an oblate spheroid in a Newtonian channel flow

To conclude the validation study, we examine the lateral migration of an oblate spheroid in a Newtonian planar channel flow and compare our results with existing literature. The spheroid is characterised by an aspect ratio of $AR = 1/2$ and a confinement ratio of $\kappa = 0.3$. The channel Reynolds number is set to $Re = 22$. Initially, the particle is released from rest at a wall-normal position of $z_0/(2H) = 0.2$ with an orientation axis $\mathbf{n} = (0.75, 0.66, 0)$. Periodic boundary conditions are employed in both the streamwise (y) and spanwise (x) directions, while a no-slip condition is imposed on the channel walls located at the z -axis. Figure 16(a) illustrates the initial and equilibrium configurations of the spheroid in the yz -plane. The background contours represent the streamwise velocity field (V). Driven by wall-induced lift forces, the particle migrates away from the boundary towards an equilibrium position located between the channel centreline and the wall. This behaviour is consistent with the classical Segré–Silberberg effect observed in the inertial migration of non-spherical particles, as previously characterised by Lashgari *et al.* (2017) and Nizkaya *et al.* (2020). The equilibrium state in the xz -plane is shown in panel (b). The spheroid eventually aligns its axis of symmetry with the vorticity direction (the x -axis), resulting in a steady-state orientation of $\mathbf{n} = (1, 0, 0)$. This alignment perfectly matches the steady-state orientations reported by Nizkaya *et al.* (2020) for similar flow conditions. Finally, panel (c) provides a quantitative comparison of the particle’s trajectory, plotting the wall-normal position as a function of the downstream streamwise coordinate. Our numerical results demonstrate great agreement with the data from Nizkaya *et al.* (2020), accurately capturing both the transient migration phase and the final lateral equilibrium position.

Appendix B. Effect of particle shape in EVP fluids

Figure 17 presents the migration of particles with varying shapes within an EVP fluid, modelled using the Saramito–Giesekus (panels (a) and (b)) and Saramito (panel (c)) equations with an elasticity of 0.05 and $Bi = 1$. All particles have an equivalent diameter of 1. In the case of the Saramito–Giesekus fluid (a,b), shear-thinning effects drive the particles towards the duct walls. The oblate particle adopts an orientation nearly perpendicular to the duct diagonal, as detailed in § 3.4. The prolate particle migrates even closer to the wall compared with the oblate case, aligning with the flow direction

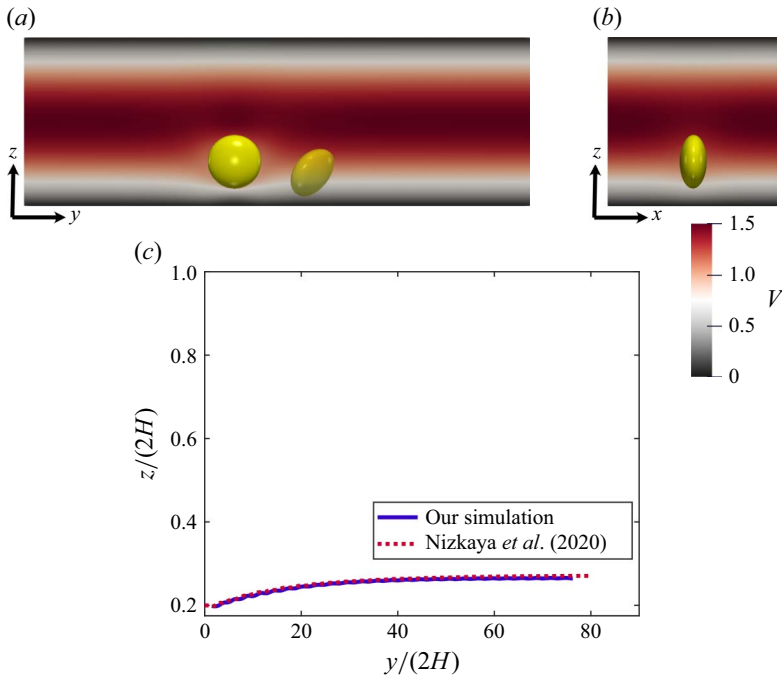


Figure 16. Inertial migration of an oblate spheroid ($AR = 1/2$) in a Newtonian planar channel flow at $Re = 22$ and $\kappa = 0.3$. (a) Particle position and orientation in the yz -plane, illustrating the transition from the initial release point to the lateral equilibrium position. Contours represent the streamwise velocity field. (b) The xz -plane showing the steady-state orientation, where the symmetry axis aligns with the vorticity direction ($\mathbf{n} = [1, 0, 0]$). (c) Quantitative comparison of the wall-normal trajectory $z/2H$ as a function of streamwise displacement ($y/(2H)$) against the result of Nizkaya *et al.* (2020).

to minimise its frontal area. The spherical particle is also displaced towards the upper wall, eventually making contact due to wall-directed inertial forces overcoming the wall-repulsion effects.

In Saramito EVP fluids, particles of all shapes tend to migrate towards the duct centre, ultimately entering the central plug region. This inward migration is driven by elastic effects that exceed a critical elasticity threshold ($El = 0.05$ for the given confinement ratio). Oblate particles with aspect ratios of $1/2$ and $1/3$ exhibit a dynamics comparable to that shown in figure 6(a, b), and their final orientations are therefore omitted for brevity. Spherical particles become fully centred within the plug, aligning closely with its width. Prolate particles also migrate towards the core but, once inside the plug, their rotational motion ceases, and they are advected downstream at a constant velocity. In contrast to VE fluids, where particles consistently orient with their smallest surface area facing the flow to minimise drag, orientation in EVP fluids is not uniquely prescribed. Instead, it depends on both the particle initial position and orientation, which influence the angle at which it enters the plug region. For example, while a prolate particle in a VE fluid aligns with its minimal cross-sectional area facing the flow, in Saramito EVP fluids – as illustrated in panel (c) – it adopts a different, non-minimal orientation.

Appendix C. Collision model and lubrication correction

Here, we summarise the key aspects of the collision model and the lubrication correction, following the formulations presented in Costa *et al.* (2015) and Ardekani *et al.* (2016).

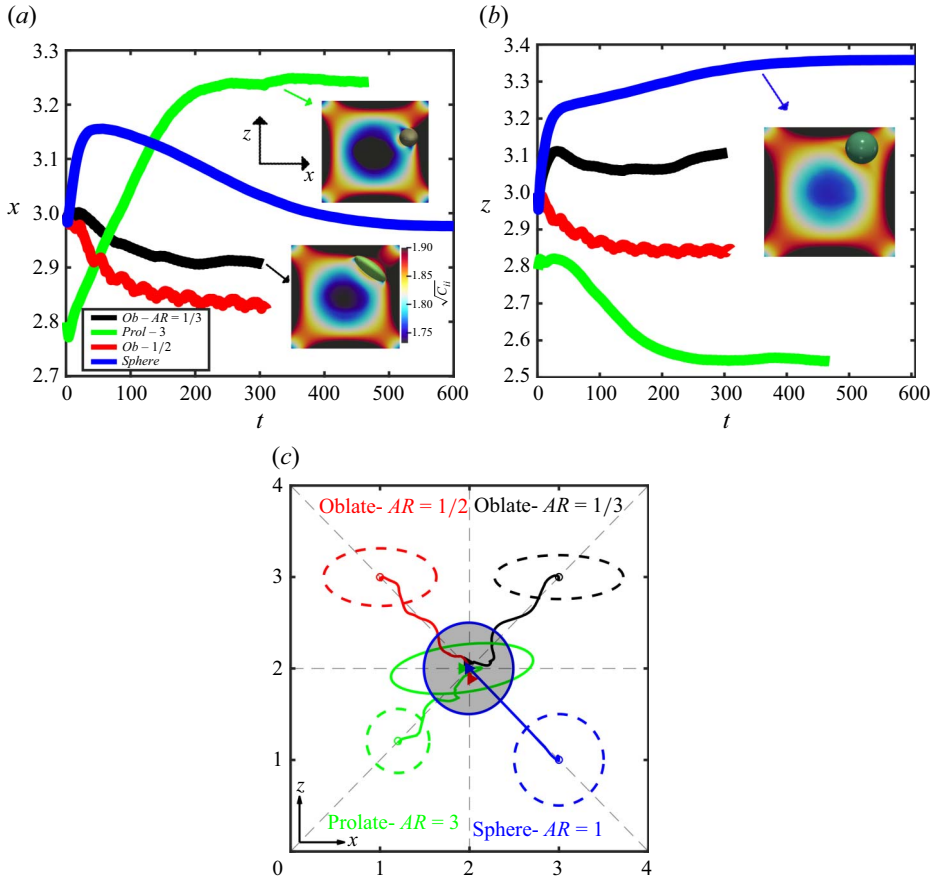


Figure 17. Particle migration in an EVP fluid with $El = 0.05$ and $Bi = 1$ for different particle shapes. (a, b) Spanwise (x) and vertical (z) trajectories of oblate, spherical and prolate particles in a Saramito–Giesekus fluid. The insets display final particle positions in the duct cross-section, overlaid on contours of square root of the trace of conformation tensor representing polymer chain stretch. (c) Cross-sectional trajectories of the same particles in a duct flow of an EVP fluid modelled by the Saramito constitutive equation.

C.1. Collision model

To account for solid–solid interactions, we employ a soft-sphere collision model proposed by Costa *et al.* (2015). This model is based on a linear spring–dashpot system acting in both normal and tangential directions, integrated with a Coulomb friction slider. While originally formulated for spherical particles, the model is extended to spheroids following the approach of Niazi Ardekani (2019). Near the contact point, each spheroid is locally approximated by a sphere whose radius corresponds to the local radius of curvature at the point of closest approach. This equivalent sphere is assigned the same mass as the original spheroid, allowing the use of analytical contact mechanics derived for spherical bodies. The normal contact force, $\mathbf{F}_{ij,n}$, acting on particle i due to contact with particle j , is directed along the line of centres $\mathbf{n}_{ij} = (\mathbf{x}_j - \mathbf{x}_i)/\|\mathbf{x}_j - \mathbf{x}_i\|$. This force is determined by the overlap distance $\delta_{ij,n}$ and the relative normal velocity $\mathbf{u}_{ij,n}$ at the contact point

$$\mathbf{F}_{ij,n} = -k_n \delta_{ij,n} - \eta_n \mathbf{u}_{ij,n}. \quad (C1)$$

The stiffness coefficient k_n and the damping coefficient η_n are determined by modelling the collision as a linear harmonic oscillator (Van der Hoef, van Sint Annaland & Kuipers

2004). To maintain numerical stability and allow the fluid solver to adapt to the change in particle momentum, the collision time T_n is set as a fixed multiple of the simulation time step, $T_n = N \Delta t$. Following the sensitivity analyses of Costa *et al.* (2015), we set $N = 8$. The spring and dashpot coefficients are expressed as

$$k_n = \frac{m_e(\pi^2 + \ln^2 e_{n,d})}{(N \Delta t)^2}, \tag{C2}$$

$$\eta_n = -\frac{2m_e \ln e_{n,d}}{N \Delta t}, \tag{C3}$$

where $m_e = (m_i^{-1} + m_j^{-1})^{-1}$ is the reduced mass and $e_{n,d}$ is the dry coefficient of restitution and is set to 0.97 in this study.

The tangential contact force, $\mathbf{F}_{ij,t}$, and torque, $\mathbf{T}_{ij,t}$, is modelled using a similar spring–dashpot framework to represent the resistance to sliding and rolling. To distinguish between sticking and sliding regimes, the tangential force is regularised by a Coulomb friction law

$$\mathbf{F}_{ij,t} = \min(\| -k_t \delta_{ij,t} - \eta_t \mathbf{u}_{ij,t} \|, \| -\mu_c \mathbf{F}_{ij,n} \|) \mathbf{t}_{ij}, \tag{C4}$$

where μ_c is the friction coefficient (fixed at 0.15), $\delta_{ij,t}$ is the tangential displacement and \mathbf{t}_{ij} is the tangential unit vector. The tangential coefficients k_t and η_t are obtained by solving the harmonic oscillator equations under the requirement that the tangential and normal collision times match ($T_t = T_n$) (Costa *et al.* 2015)

$$k_t = \frac{m_{e,t}(\pi^2 + \ln^2 e_{t,d})}{(N \Delta t)^2}, \quad \eta_t = -\frac{2m_{e,t} \ln e_{t,d}}{N \Delta t}, \tag{C5}$$

where $e_{t,d}$ is the dry tangential coefficient of restitution, which, like the normal coefficient $e_{n,d}$, is a prescribed input parameter of the model and is set to 0.1. The effective tangential reduced mass, $m_{e,t}$, accounts for the rotational inertia of the colliding bodies and is defined as

$$m_{e,t} = \left(1 + \frac{1}{K^2}\right)^{-1} m_e, \tag{C6}$$

where K denotes the normalised radius of gyration for the approximating spheres ($K^2 = 2/5$ for a homogeneous solid sphere).

Whenever the tangential force exceeds the Coulomb limit, the displacement is saturated to ensure physical consistency with the sliding regime (Costa *et al.* 2015).

The total collision force \mathbf{F}_i^c and torque \mathbf{T}_i^c exerted on particle i are computed as the sum of all individual contact contributions and are added to the right-hand side of the Newton–Euler equations (see (2.5) and (2.6)) to resolve the particle motion. Particle–wall interactions are treated as the limiting case of a collision with a sphere of infinite radius. In this limit, the reduced mass simplifies to $m_e = m_i$ and the overlap $\delta_{iw,n}$ is defined relative to the planar wall surface. For further details regarding the collision model, the reader is referred to the work of Costa *et al.* (2015).

C.2. Lubrication model

A particle immersed in a viscous fluid experiences significant lubrication forces when approaching another body, such as a wall or another particle. These forces, which arise from the drainage of the fluid film within the gap, can be described by the analytical asymptotic solutions of Jeffrey (1982) for spheres of different radii in the Stokes regime. While the IBM inherently resolves these hydrodynamic interactions, it underestimates the

lubrication resistance when the gap width falls below the Eulerian grid resolution, Δx (Breugem 2010). To avoid the high computational cost of mesh refinement, we apply a lubrication correction to compensate for the under-resolved pressure in the narrow gap. The dominant lubrication component is the normal squeezing force, which scales with $1/\epsilon$ (where ϵ is the normalised gap width). In contrast, the tangential and rotational components diverge only logarithmically ($\ln \epsilon$) and have a negligible impact on the overall contact dynamics (Simões Costa 2017).

Similar to the collision model, spheroidal particles are locally approximated near the contact point by spheres with a radius equal to the local radius of curvature (Niazi Ardekani 2019). The normal squeezing force is the dominant lubrication component, as it scales with $1/\epsilon$, whereas tangential and rotational terms diverge only logarithmically ($\ln \epsilon$) and were found to have negligible influence on contact dynamics (Costa *et al.* 2015).

For gap widths below a resolution threshold, $\epsilon < \epsilon_{\Delta x}$, a correction force \mathbf{F}_{lub} is incorporated into the Newton–Euler equations according to Jeffrey (1982)

$$\mathbf{F}_{lub} = -6\pi\mu R_i \mathbf{u}_{ij,n} [\lambda(\kappa, \epsilon) - \lambda(\kappa, \epsilon_{\Delta x})], \quad (\text{C7})$$

where R_i is the local radius of curvature, κ is the curvature ratio and λ is the Stokes amplification factor. To prevent the unphysical divergence of the force as $\epsilon \rightarrow 0$, the amplification is saturated at a roughness length scale ϵ_σ , representing contact through surface asperities: $\lambda(\kappa, \epsilon < \epsilon_\sigma) = \lambda(\kappa, \epsilon_\sigma)$ (Costa *et al.* 2015).

In this study, the resolution thresholds are prescribed as $\epsilon_{\Delta x} = 0.025$ for particle–particle interactions and $\epsilon_{\Delta x} = 0.05$ for particle–wall interactions. The value of $\epsilon_{\Delta x}$ is determined by simulating a sphere slowly approaching towards a planar wall or between two spheres, and identifying the gap below which the IBM no longer accurately resolves the lubrication interaction. The lubrication correction defined in (C7) is activated only when the gap falls below these specific separations. To account for surface asperities and prevent the unphysical divergence of the lubrication force at contact, a constant roughness cutoff of $\epsilon_\sigma = 0.001$ is applied to both particle–particle and particle–wall interactions, following the regularisation proposed by Costa *et al.* (2015).

REFERENCES

- ABTAHI, S.A. & ELFRING, G.J. 2019 Jeffery orbits in shear-thinning fluids. *Phys. Fluids* **31** (10), 103106.
- AMINI, H., LEE, W. & DI CARLO, D. 2014 Inertial microfluidic physics. *Lab on a Chip* **14** (15), 2739–2761.
- ARDEKANI, M.N., COSTA, P., BREUGEM, W.P. & BRANDT, L. 2016 Numerical study of the sedimentation of spheroidal particles. *Intl J. Multiphase Flow* **87**, 16–34.
- ASMOLOV, E.S. 1999 The inertial lift on a spherical particle in a plane poiseuille flow at large channel reynolds number. *J. Fluid Mech.* **381**, 63–87.
- BALMFORTH, N.J., FRIGAARD, I.A. & OVARLEZ, G. 2014 Yielding to stress: recent developments in viscoplastic fluid mechanics. *Annu. Rev. Fluid Mech.* **46** (1), 121–146.
- BARBATI, A.C., DESROCHES, J., ROBISSON, A. & MCKINLEY, G.H. 2016 Complex fluids and hydraulic fracturing. *Ann. Rev. Chem. Biomed. Engng* **7**, 415–453.
- BARTRAM, E., GOLDSMITH, H.L. & MASON, S.G. 1975 Particle motions in non-newtonian media: iii. further observations in elasticoviscous fluids. *Rheol. Acta* **14**, 776–782.
- BREUGEM, W.-P. 2010 A combined soft-sphere collision/immersed boundary method for resolved simulations of particulate flows, In *Fluids Engineering Division Summer Meeting*, vol. 49484, pp. 2381–2392.
- BREUGEM, W.-P. 2012 A second-order accurate immersed boundary method for fully resolved simulations of particle-laden flows. *J. Comput. Phys.* **231** (13), 4469–4498.
- CHAPARIAN, E., ARDEKANI, M.N., BRANDT, L. & TAMMISOLA, O. 2020a Particle migration in channel flow of an elastoviscoplastic fluid. *J. Non-Newtonian Fluid Mech.* **284**, 104376.
- CHAPARIAN, E., IZBASSAROV, D., DE VITA, F., BRANDT, L. & TAMMISOLA, O. 2020b Yield-stress fluids in porous media: a comparison of viscoplastic and elastoviscoplastic flows. *Meccanica* **55**, 331–342.
- CHEDDADI, I., SARAMITO, P., DOLLET, B., RAUFASTE, C. & GRANER, F. 2011 Understanding and predicting viscous, elastic, plastic flows. *Eur. Phys. J. E* **34**, 1–15.

- CHOI, Y.-S., SEO, K.-W. & LEE, S.-J. 2011 Lateral and cross-lateral focusing of spherical particles in a square microchannel. *Lab on a Chip* **11** (3), 460–465.
- CHUN, B.A.J.C. & LADD, A.J.C. 2006 Inertial migration of neutrally buoyant particles in a square duct: an investigation of multiple equilibrium positions. *Phys. Fluids* **18** (3), 031704.
- COSTA, P. 2018 A FFT-based finite-difference solver for massively-parallel direct numerical simulations of turbulent flows. *Comput. Math. Appl.* **76** (8), 1853–1862.
- COSTA, P., BOERSMA, B.J., WESTERWEEL, J. & BREUGEM, W.-P. 2015 Collision model for fully resolved simulations of flows laden with finite-size particles. *Phys. Rev. E* **92** (5), 053012.
- DABADE, V., MARATH, N.K. & SUBRAMANIAN, G. 2015 Effects of inertia and viscoelasticity on sedimenting anisotropic particles. *J. Fluid Mech.* **778**, 133–188.
- D'AVINO, G., GRECO, F. & MAFFETTONE, P.L. 2017 Particle migration due to viscoelasticity of the suspending liquid and its relevance in microfluidic devices. *Annu. Rev. Fluid Mech.* **49**, 341–360.
- D'AVINO, G., HULSEN, M.A., GRECO, F. & MAFFETTONE, P.L. 2014 Bistability and metastability scenario in the dynamics of an ellipsoidal particle in a sheared viscoelastic fluid. *Phys. Rev. E* **89** (4), 043006.
- DE VITA, F., ROSTI, M.E., IZBASSAROV, D., DUFFO, L.T., OUTI, H.S. & BRANDT, L. 2018 Elastoviscoplastic flows in porous media. *J. Non-Newtonian Fluid Mech.* **258**, 10–21.
- DI CARLO, D. 2009 Inertial microfluidics. *Lab on a Chip* **9** (21), 3038–3046.
- DI CARLO, D., EDD, J.F., HUMPHRY, K.J., STONE, H.A. & TONER, M. 2009 Particle segregation and dynamics in confined flows. *Phys. Rev. Lett.* **102** (9), 094503.
- DI CARLO, D., IRIMIA, D., TOMPKINS, R.G. & TONER, M. 2007 Continuous inertial focusing, ordering, and separation of particles in microchannels. *Proc. Natl Acad. Sci.* **104** (48), 18892–18897.
- DI GIUSTO, D., BERGOUNOUX, L., MARCHIOLI, C. & GUAZZELLI, É. 2024 Influence of small inertia on jeffery orbits. *J. Fluid Mech.* **979**, A42.
- EINARSSON, J., CANDELIER, F., LUNDELL, F., ANGILELLA, J.R. & MEHLIG, B. 2015 Rotation of a spheroid in a simple shear at small Reynolds number. *Phys. Fluids* **27** (6), 063301.
- EOM, W., *et al.* 2025 Fast 3D printing of fine, continuous, and soft fibers via embedded solvent exchange. *Nat. Commun.* **16** (1), 842.
- EWOLDT, R.H. & MCKINLEY, G.H. 2017 Mapping thixo-elasto-visco-plastic behavior. *Rheol. Acta* **56**, 195–210.
- FATAEI, S. 2022 Flow-induced particle migration in concrete under high shear rates. Master's thesis, Dresden University of Technology, Dresden.
- FRAGGEDAKIS, D., DIMAKOPOULOS, Y. & TSAMOPOULOS, J. 2016 Yielding the yield-stress analysis: a study focused on the effects of elasticity on the settling of a single spherical particle in simple yield-stress fluids. *Soft Matt.* **12** (24), 5378–5401.
- GAUTHIER, F., GOLDSMITH, H.L. & MASON, S.G. 1971 Particle motions in non-newtonian media. II. Poiseuille flow. *Trans. Soc. Rheol.* **15** (2), 297–330.
- GIESEKUS, H. 1982 A simple constitutive equation for polymer fluids based on the concept of deformation-dependent tensorial mobility. *J. Non-Newtonian Fluid Mech.* **11** (1–2), 69–109.
- GOYAL, N. & DERKSEN, J.J. 2012 Direct simulations of spherical particles sedimenting in viscoelastic fluids. *J. Non-Newtonian Fluid Mech.* **183**, 1–13.
- GRATTON, S.E.A., ROPP, P.A., POHLHAUS, P.D., LUFT, J.C., MADDEN, V.J., NAPIER, M.E. & DESIMONE, J.M. 2008 The effect of particle design on cellular internalization pathways. *Proc. Natl Acad. Sci.* **105** (33), 11613–11618.
- GUNES, D.Z., SCIROCCO, R., MEWIS, J. & VERMANT, J. 2008 Flow-induced orientation of non-spherical particles: effect of aspect ratio and medium rheology. *J. Non-Newtonian Fluid Mech.* **155** (1–2), 39–50.
- HABIBI, S. 2026 Numerical study of particle suspensions in non-newtonian fluids. PhD thesis, KTH Royal Institute of Technology.
- HABIBI, S., IQBAL, K.T., ARDEKANI, M.N., CHAPARIAN, E., BRANDT, L. & TAMMISOLA, O. 2025 Numerical study of particle suspensions in duct flow of elastoviscoplastic fluids. *J. Fluid Mech.* **1007**, A36.
- HAFEMANN, T. & FRÖHLICH, J. 2023 Inertial migration of non-spherical particles in straight microfluidic channels. *Phys. Fluids* **35** (1), 013328.
- HO, B.P. & LEAL, L.G. 1974 Inertial migration of rigid spheres in two-dimensional unidirectional flows. *J. Fluid Mech.* **65** (2), 365–400.
- HO, B.P. & LEAL, L.G. 1976 Migration of rigid spheres in a two-dimensional unidirectional shear flow of a second-order fluid. *J. Fluid Mech.* **76** (4), 783–799.
- VAN DER HOEF, M.A., VAN SINT ANNALAND, M. & KUIPERS, J.A.M. 2004 Computational fluid dynamics for dense gas–solid fluidized beds: a multi-scale modeling strategy. *Chem. Engng Sci.* **59** (22–23), 5157–5165.

- HOLENBERG, Y., LAVRENTEVA, O.M., SHAVIT, U. & NIR, A. 2012 Particle tracking velocimetry and particle image velocimetry study of the slow motion of rough and smooth solid spheres in a yield-stress fluid. *Phys. Rev. E* **86** (6), 066301.
- HU, X., LIN, J., ZHU, Z., YU, Z., LIN, Z. & LI, X. 2024 Elasto-inertial focusing and rotating characteristics of ellipsoidal particles in a square channel flow of oldroyd-b viscoelastic fluids. *J. Fluid Mech.* **997**, A32.
- HUR, S.C., CHOI, S.-E., KWON, S. & CARLO, D.D. 2011 Inertial focusing of non-spherical microparticles. *Appl. Phys. Lett.* **99** (4), 044101.
- IZBASSAROV, D., ROSTI, M.E., ARDEKANI, M.N., SARABIAN, M., HORMOZI, S., BRANDT, L. & TAMMISOLA, O. 2018 Computational modeling of multiphase viscoelastic and elastoviscoplastic flows. *Intl J. Numer. Meth. Flow* **88** (12), 521–543.
- IZBASSAROV, D., ROSTI, M.E., BRANDT, L. & TAMMISOLA, O. 2021 Effect of finite weissenberg number on turbulent channel flows of an elastoviscoplastic fluid. *J. Fluid Mech.* **927**, A45.
- IZBASSAROV, D. & TAMMISOLA, O. 2020 Dynamics of an elastoviscoplastic droplet in a newtonian medium under shear flow. *Phys. Rev. Fluids* **5** (11), 113301.
- JEFFERY, G.B. 1922 The motion of ellipsoidal particles immersed in a viscous fluid. *Proc. R. Soc. Lond. Series A Contain. Papers Math. Phys. Char.* **102** (715), 161–179.
- JEFFREY, D.J. 1982 Low-Reynolds-number flow between converging spheres. *Mathematika* **29** (1), 58–66.
- KAZAROONI, H.T., FORNARI, W., HUSSONG, J. & BRANDT, L. 2017 Inertial migration in dilute and semidilute suspensions of rigid particles in laminar square duct flow. *Phys. Rev. Fluids* **2** (8), 084301.
- LANGELLA, A., FRANZINO, G., MAFFETONE, P.L., LAROBINA, D. & D'AVINO, G. 2023 Dynamics of non-spherical particles in viscoelastic fluids flowing in a microchannel. *Soft Matt.* **19** (48), 9541–9549.
- LASHGARI, I., ARDEKANI, M.N., BANERJEE, I., RUSSOM, A. & BRANDT, L. 2017 Inertial migration of spherical and oblate particles in straight ducts. *J. Fluid Mech.* **819**, 540–561.
- LEAL, L.G. 1975 The slow motion of slender rod-like particles in a second-order fluid. *J. Fluid Mech.* **69** (2), 305–337.
- LESHANSKY, A.M., BRANSKY, A., KORIN, N. & DINNAR, U. 2007 Tunable nonlinear viscoelastic ‘focusing’ in a microfluidic device. *Phys. Rev. Lett.* **98** (23), 234501.
- LI, G., MCKINLEY, G.H. & ARDEKANI, A.M. 2015 Dynamics of particle migration in channel flow of viscoelastic fluids. *J. Fluid Mech.* **785**, 486–505.
- LI, M.-Z., HE, Y.-P., LIU, W.-H., LIU, Y.-D., HUANG, C. & JIANG, R.-H. 2020 Effect of adding finer particles on the transport characteristics of coarse-particle slurries in pipelines. *Ocean Engng* **218**, 108160.
- LI, Y., XU, C. & ZHAO, L. 2023a Fluid-inertia torque on spheroids in pseudo-plastic fluid flows: effect of shear-thinning rheology. *J. Fluid Mech.* **970**, A12.
- LI, Y., XU, C. & ZHAO, L. 2023b Rotational dynamics of a neutrally buoyant prolate spheroid in viscoelastic shear flows at finite Reynolds numbers. *J. Fluid Mech.* **958**, A20.
- LI, Y., XU, C. & ZHAO, L. 2024 Oscillation migration of a neutrally buoyant oblate spheroid in the elastoinertial duct flow. *J. Fluid Mech.* **997**, A57.
- LIU, C., XUE, C., CHEN, X., SHAN, L., TIAN, Y. & HU, G. 2015 Size-based separation of particles and cells utilizing viscoelastic effects in straight microchannels. *Anal. Chem.* **87** (12), 6041–6048.
- LIU, P., LIU, H., SEMENEC, L., YUAN, D., YAN, S., CAIN, A.K. & LI, M. 2022 Length-based separation of bacillus subtilis bacterial populations by viscoelastic microfluidics. *Microsyst. Nanoengng* **8** (1), 7.
- LOPEZ, W.F., NACCACHE, M.F., DE SOUZA, M. & PAULO, R. 2018 Rising bubbles in yield stress materials. *J. Rheol.* **62** (1), 209–219.
- LORMAND, B.M. & PHILLIPS, R.J. 2004 Sphere migration in oscillatory couette flow of a viscoelastic fluid. *J. Rheol.* **48** (3), 551–570.
- LU, X., ZHU, L., HUA, R.-M. & XUAN, X. 2015 Continuous sheath-free separation of particles by shape in viscoelastic fluids. *Appl. Phys. Lett.* **107** (26).
- MARTEL, J.M. & TONER, M. 2014 Inertial focusing in microfluidics. *Annu. Rev. Biomed. Engng* **16**, 371.
- MASAEI, M., SOLLIER, E., AMINI, H., MAO, W., CAMACHO, K., DOSHI, N., MITRAGOTRI, S., ALEXEEV, A. & DI CARLO, D. 2012 Continuous inertial focusing and separation of particles by shape. *Phys. Rev. X* **2** (3), 031017.
- MATAS, J.-P., MORRIS, J.F. & GUAZZELLI, É. 2004 Inertial migration of rigid spherical particles in poiseuille flow. *J. Fluid Mech.* **515**, 171–195.
- MITRAGOTRI, S. & LAHANN, J. 2009 Physical approaches to biomaterial design. *Nat. Mater.* **8** (1), 15–23.
- MITTAL, R. & IACCARINO, G. 2005 Immersed boundary methods. *Annu. Rev. Fluid Mech.* **37**, 239–261.
- MIURA, K., ITANO, T. & SUGIHARA-SEKI, M. 2014 Inertial migration of neutrally buoyant spheres in a pressure-driven flow through square channels. *J. Fluid Mech.* **749**, 320–330.
- NAIAZI ARDEKANI, M. 2019 Numerical study of transport phenomena in particle suspensions. PhD thesis, KTH Royal Institute of Technology.

- NIZKAYA, T.V., GEKOVA, A.S., HARTING, J., ASMOLOV, E.S. & VINOGRADOVA, O.I. 2020 Inertial migration of oblate spheroids in a plane channel. *Phys. Fluids* **32** (11), 112017.
- OLDROYD, J.G. 1950 On the formulation of rheological equations of state. *Proc. R. Soc. Lond. Series A. Math. Phys. Sci.* **200** (1063), 523–541.
- PÉMÉJA, J., GÉRAUD, B., BARENTIN, C. & LE MERRER, M. 2019 Wall slip regimes in jammed suspensions of soft microgels. *Phys. Rev. Fluids* **4** (3), 033301.
- POURZAHEDI, A., ZARE, M. & FRIGAARD, I.A. 2021 Eliminating injection and memory effects in bubble rise experiments within yield stress fluids. *J. Non-Newtonian Fluid Mech.* **292**, 104531.
- PUTZ, A.M.V., BURGHELEA, T.I., FRIGAARD, I.A. & MARTINEZ, D.M. 2008 Settling of an isolated spherical particle in a yield stress shear thinning fluid. *Phys. Fluids* **20** (3), 033102.
- ROSÉN, T. 2016 Angular dynamics of non-spherical particles in linear flows related to production of biobased materials. PhD thesis, KTH Royal Institute of Technology.
- ROSÉN, T., LUNDELL, F. & AIDUN, C.K. 2014 Effect of fluid inertia on the dynamics and scaling of neutrally buoyant particles in shear flow. *J. Fluid Mech.* **738**, 563–590.
- ROSTI, M.E., IZBASSAROV, D., TAMMISOLA, O., HORMOZI, S. & BRANDT, L. 2018 Turbulent channel flow of an elastoviscoplastic fluid. *J. Fluid Mech.* **853**, 488–514.
- SAFFMAN, P.G. 1956 On the motion of small spheroidal particles in a viscous liquid. *J. Fluid Mech.* **1** (5), 540–553.
- SARABIAN, M., ROSTI, M.E., BRANDT, L. & HORMOZI, S. 2020 Numerical simulations of a sphere settling in simple shear flows of yield stress fluids. *J. Fluid Mech.* **896**, A17.
- SARAMITO, P. 2007 A new constitutive equation for elastoviscoplastic fluid flows. *J. Non-Newtonian Fluid Mech.* **145** (1), 1–14.
- SARAMITO, P. 2009 A new elastoviscoplastic model based on the herschel–bulkley viscoplastic model. *J. Non-Newtonian Fluid Mech.* **158** (1–3), 154–161.
- SARAMITO, P. 2016 *Complex Fluids*. Springer.
- SCHWEIZER, K.S. & XIE, S.-J. 2018 Physics of the stress overshoot and chain stretch dynamics of entangled polymer liquids under continuous startup nonlinear shear. *ACS Macro Lett.* **7** (2), 218–222.
- SEGRÉ, G. & SILBERBERG, A. 1961 Radial particle displacements in poiseuille flow of suspensions. *Nature* **189** (4760), 209–210.
- SEGRÉ, G. & SILBERBERG, A. 1962 Behaviour of macroscopic rigid spheres in poiseuille flow part 1. Determination of local concentration by statistical analysis of particle passages through crossed light beams. *J. Fluid Mech.* **14** (1), 115–135.
- SHAQFEH, E.S.G. 2019 On the rheology of particle suspensions in viscoelastic fluids. *AIChE J.* **65** (5), e16575.
- SHU, C.-W. 2009 High order weighted essentially nonoscillatory schemes for convection dominated problems. *SIAM Rev.* **51** (1), 82–126.
- SIMÕES COSTA, P. 2017 *Interface-Resolved Simulations of Dense Turbulent Suspension Flows*. Dissertation (tu delft), Delft University of Technology.
- SNIJKERS, F., D’AVINO, G., MAFFETTONE, P.L., GRECO, F., HULSEN, M.A. & VERMANT, J. 2011 Effect of viscoelasticity on the rotation of a sphere in shear flow. *J. Non-Newtonian Fluid Mech.* **166** (7–8), 363–372.
- STOECKLEIN, D. & DI CARLO, D. 2018 Nonlinear microfluidics. *Anal. Chem.* **91** (1), 296–314.
- TAI, C.-W. & NARSIMHAN, V. 2022 Experimental and theoretical studies of cross-stream migration of non-spherical particles in a quadratic flow of a viscoelastic fluid. *Soft Matt.* **18** (24), 4613–4624.
- TAI, C.-W., WANG, S. & NARSIMHAN, V. 2020a Cross-stream migration of non-spherical particles in a second-order fluid—theories of particle dynamics in arbitrary quadratic flows. *J. Fluid Mech.* **895**, A6.
- TAI, C.-W., WANG, S. & NARSIMHAN, V. 2020b Cross-stream migration of nonspherical particles in second-order fluid flows: effect of flow profiles. *AIChE J.* **66** (12), e17076.
- TAKEISHI, N. & IMAI, Y. 2017 Capture of microparticles by bolus flow of red blood cells in capillaries. *Sci. Rep.* **7** (1), 5381.
- TANRIVERDI, S., CRUZ, J., HABIBI, S., AMINI, K., COSTA, M., LUNDELL, F., MÅRTENSSON, G., BRANDT, L., TAMMISOLA, O. & RUSSOM, A. 2024 Elasto-inertial focusing and particle migration in high aspect ratio microchannels for high-throughput separation. *Microsyst. Nanoengng* **10** (1), 87.
- TANRIVERDI, S., *et al.* 2025 Sheathless elasto-inertial focusing of sub-25 Nm particles in straight microchannels. *Small* **21**, 2503369.
- TSENG, H.-C. 2021 A constitutive analysis of stress overshoot for polymer melts under startup shear flow. *Phys. Fluids* **33** (5), 051706.
- USPAL, W.E., BURAK ERAL, H. & DOYLE, P.S. 2013 Engineering particle trajectories in microfluidic flows using particle shape. *Nat. Commun.* **4** (1), 2666.

- VILLONE, M.M., D'AVINO, G., HULSEN, M.A., GRECO, F. & MAFFETTONE, P.L. 2013 Particle motion in square channel flow of a viscoelastic liquid: migration vs. secondary flows. *J. Non-Newtonian Fluid Mech.* **195**, 1–8.
- VOTH, G.A. & SOLDATI, A. 2017 Anisotropic particles in turbulence. *Annu. Rev. Fluid Mech.* **49** (1), 249–276.
- WANG, Y., YU, Z. & LIN, J. 2019 Numerical simulations of the motion of ellipsoids in planar couette flow of giesekus viscoelastic fluids. *Microfluid. Nanofluid.* **23**, 1–16.
- WON, D. & KIM, C. 2004 Alignment and aggregation of spherical particles in viscoelastic fluid under shear flow. *J. Non-Newtonian Fluid Mechan.* **117** (2–3), 141–146.
- YOUNES, E., BERTOLA, V., CASTELAIN, C. & BURGHELEA, T. 2020 Slippery flows of a carbopol gel in a microchannel. *Phys. Rev. Fluids* **5** (8), 083303.
- YUE, P., DOOLEY, J. & FENG, J.J. 2008 A general criterion for viscoelastic secondary flow in pipes of noncircular cross section. *J. Rheol.* **52** (1), 315–332.
- ZADE, S., SHAMU, T.J., LUNDELL, F. & BRANDT, L. 2020 Finite-size spherical particles in a square duct flow of an elastoviscoplastic fluid: an experimental study. *J. Fluid Mech.* **883**, A6.
- ZENG, L., BALACHANDAR, S. & FISCHER, P. 2005 Wall-induced forces on a rigid sphere at finite Reynolds number. *J. Fluid Mech.* **536**, 1–25.
- ZHOU, J. & PAPAUTSKY, I. 2020 Viscoelastic microfluidics: progress and challenges. *Microsyst. Nanoengng* **6** (1), 1–24.